

See discussions, stats, and author profiles for this publication at: <https://www.researchgate.net/publication/9052676>

# Molecular Dynamics Simulation of Dark-adapted Rhodopsin in an Explicit Membrane Bilayer: Coupling between Local Retinal and Larger Scale Conformational Change

ARTICLE in JOURNAL OF MOLECULAR BIOLOGY · NOVEMBER 2003

Impact Factor: 4.33 · DOI: 10.1016/j.jmb.2003.08.045 · Source: PubMed

---

CITATIONS

102

---

READS

21

4 AUTHORS, INCLUDING:



Thomas B Woolf

Johns Hopkins Medicine

70 PUBLICATIONS 1,905 CITATIONS

SEE PROFILE

# Molecular Dynamics Simulation of Dark-adapted Rhodopsin in an Explicit Membrane Bilayer: Coupling between Local Retinal and Larger Scale Conformational Change

Paul S. Crozier<sup>1</sup>, Mark J. Stevens<sup>1\*</sup>, Lucy R. Forrest<sup>2</sup> and Thomas B. Woolf<sup>2</sup>

<sup>1</sup>Sandia National Laboratories  
P.O. Box 5800, MS 1411  
Albuquerque, NM 87185-1411  
USA

<sup>2</sup>Department of Physiology  
Johns Hopkins University  
School of Medicine, Baltimore  
MD 21205, USA

The light-driven photocycle of rhodopsin begins the photoreceptor cascade that underlies visual response. In a sequence of events, the retinal covalently attached to the rhodopsin protein undergoes a conformational change that communicates local changes to a global conformational change throughout the whole protein. In turn, the large-scale protein change then activates G-proteins and signal amplification throughout the cell. The nature of this change, involving a coupling between a local process and larger changes throughout the protein, may be important for many membrane proteins. In addition, functional work has shown that this coupling occurs with different efficiency in different lipid settings. To begin to understand the nature of the efficiency of this coupling in different lipid settings, we present a molecular dynamics study of rhodopsin in an explicit dioleoyl-phosphatidylcholine bilayer. Our system was simulated for 40 ns and provides insights into the very early events of the visual cascade, before the full transition and activation have occurred. In particular, we see an event near 10 ns that begins with a change in hydrogen bonding near the retinal and that leads through a series of coupled changes to a shift in helical tilt. This type of event, though rare on the molecular dynamics time-scale, could be an important clue to the types of coupling that occur between local and large-scale conformational change in many membrane proteins.

© 2003 Elsevier Ltd. All rights reserved.

\*Corresponding author

**Keywords:** rhodopsin; molecular dynamics; membrane protein; simulation

## Introduction

Rhodopsin is the prototypical G-protein coupled receptor (GPCR) due to the large amount of experimental information related to both its structure and its function.<sup>1–5</sup> It is also the first GPCR with a defined tertiary structure and is thus an excellent candidate for trying to understand the molecular details of function. A full understanding of these

details is difficult, however, due to the large separation in time-scales between the photocycle of rhodopsin and current computational limits in computer simulation of bio-molecules. In particular, the full photocycle occurs on the millisecond time-scale,<sup>6</sup> while the state-of-the-art in computer simulation of large proteins is tens of nanoseconds.

Despite the limitations on accessible conformations for biomolecules within a computer-simulated system, many important questions can be addressed through detailed computational models that would not be directly measured experimentally. Thus, a detailed computational model can suggest details of function and motion that are difficult to envision from a static structure and isolated experiments. That is, simulation can play a valuable role in helping to inform intuition about how a structure moves in its native environment and in suggesting

Present address: L. Forrest, Department of Biochemistry, University of Columbia, New York, NY 10032, USA.

Abbreviations used: GPCR, G-protein coupled receptor; DOPC, dioleoylphosphatidylcholine; vdW, van der Waals.

E-mail address of the corresponding author: msteve@sandia.gov

new classes of experiments that would not have been attempted in the absence of a detailed simulation.

In addition to the many intriguing features related to the rhodopsin photocycle, rhodopsin is also the first membrane protein to show a clear sensitivity to its lipid environment. For example, the Brown group has shown that the M-I to M-II transition is modulated by the relative mixture of DOPC to DOPE lipids.<sup>7–12</sup> In addition, it has been known for some time that rhodopsin is sensitive to the alkane chain type.<sup>13,14</sup> This has led to the realization that rhodopsin prefers DHA for its environmental background.<sup>15</sup> A leading question then, in addition to the details of the photocycle, is how the lipid setting can influence the types of functionally important motions that the rhodopsin molecule can perform.

There are many excellent reviews on rhodopsin and the connections from rhodopsin to both GPCRs and retinal cell function.<sup>1–5</sup> It is not our intent to review all of the large amount of experimental information available for this system, as that would then be a full separate article in its own right. Rather, we aim in the following paragraphs to provide some further context for consideration of the computations.

## Rhodopsin background

Bovine rhodopsin has served as a model system for the understanding of transduction for many years.<sup>16</sup> In particular, studies in bovine rods have led to a general understanding of G-protein coupled systems, and have led to the first GPCR that was sequenced,<sup>16</sup> and to understanding of the connections between particular residues and the rhodopsin function.<sup>3,17</sup> For example, the role of Glu113 as the counterion,<sup>18</sup> the critical role of certain residues in transduction,<sup>19,20</sup> and initial suggestions for spectral tuning<sup>21–23</sup> all begin with rhodopsin. An upcoming frontier is the understanding of the connections between the structures of the G-protein itself<sup>24,25</sup> and the conformational changes that underlie the photocycle and lead to activation and signaling.

## Low-resolution structures of rhodopsin

Hydrophobic analysis of the rhodopsin sequence led to suggestions that the membrane protein had seven transmembrane helices.<sup>26</sup> These initial suggestions were confirmed through low-resolution structural work<sup>27</sup> that also provided the impetus for improved models of GPCRs.<sup>28</sup> The low-resolution structures were also sufficient to confirm that rhodopsin and bacteriorhodopsin do not share structural similarity and that homology models for GPCRs based on bacteriorhodopsin were not correct.

## X-ray structure

Membrane proteins have proven difficult to crystallize for high-resolution structural information. Thus, each new structure brings a wave of excitement and generates a host of new questions. The rhodopsin structure showed the expected

seven transmembrane domains that had been predicted both computationally and from low-resolution data.<sup>29–33</sup> In addition, the structure showed a beta-strand cap in the extracellular loop from helices 3 to 4. This cap structure may also play a role in other family A GPCRs and suggests that the properties of the binding site may not be determined entirely by the transmembrane domains. The structure showed the existence of an eighth amphipathic helix that also has two palmitoylation sites associated with it.<sup>29</sup> While the structure is important for showing the conformation associated with the dark state and for determining the protein environment of the retinal, it does not, by itself, show how the large conformational changes occur that lead to activation of G-proteins. This structure furthermore provides the basis for consideration of homology models of other GPCRs, for consideration of packing arrangements of helices in membrane proteins and even for considerations of the folding of alpha-helical membrane proteins.<sup>34–36</sup>

## UV-FTIR spectroscopy; photocycle

The rhodopsin photocycle has been described on the basis of spectral measurements.<sup>37–41</sup> With the recent crystal structure it is possible to start relating the structure to the measurements, but this requires a quantum-mechanical framework for the computation. This relates back to early work on the relation between the energetics of the activating light and the coupling to protein and retinal conformations.<sup>42,43</sup> In particular, there has been much discussion of the role of electrostatics and of modulation by the protein environment of the retinal conformational energetics. Clearly, a full understanding of the coupling between conformation at the retinal level and the protein environmental changes due to the light activation is central to relating structure to function in this system. Two recent molecular dynamics calculations start to try to connect the *cis-trans* isomerization of the retinal with the protein changes.<sup>44,45</sup> In one simulation, starting from the dark-adapted state in a membrane setting, steered molecular dynamics is used to force the transition.<sup>45</sup> In a second simulation paper, a membrane mimic was used for the environment and restraints were applied to evaluate the *cis-trans* changes in the first stages of the photocycle.<sup>44</sup> In addition, the reaction path for the transition has been considered from a theoretical viewpoint and suggests that a hula-twist conformational change occurs during the photocycle.<sup>46–48</sup> Confirmation of the reaction mechanism has been aided by consideration of designed chemical mimics of retinal that alter the photocycle in controlled ways.<sup>49–53</sup>

## Electron paramagnetic resonance; large-scale motions

The details of how light induces a conformational

change leading to G-protein activation are not revealed by the X-ray structure or the UV-FTIR spectral methods. Some insights into the types of motions that occur with activation have been achieved through the use of cysteine-linked spin label methods.<sup>54,55</sup> With this approach an engineered cysteine is reacted with a spin-label and either distances between labels or relative accessibility of a solvent-based probe is determined.<sup>54,55</sup> The results have suggested that the photocycle involves changes in tilt and some rotation in helices III and VI.<sup>55–57</sup> This suggests that some part of the activation of rhodopsin involves coupling between a sensor of the local change in rhodopsin and the generation of large rigid-body like movements in the helices that leads to activation of G-proteins.<sup>54,55</sup> These results have also been examined and extended by looking at cysteine–cysteine interactions between engineered sites in rhodopsin.<sup>58</sup>

### Solid-state and high-resolution NMR

Rhodopsin has been used as a testing ground for measurements of distance in SS-NMR with rotational resonance and other methods.<sup>59–70</sup> The results have provided structural constraints on distances in the rhodopsin molecule and have inferred properties of the photocycle. In particular, the NMR methods have suggested the possibility that the beta ionone retinal ring may be in a *trans* rather than the *cis* state observed in the X-ray structure.<sup>70</sup> Recent, continuing analysis of this situation has suggested that there is room for either conformation, while the exact conformation of the dark-adapted state for the ring is thus unclear. In addition, NMR methods have been used to infer relative motion of different regions of rhodopsin and to suggest aspects of the lipid dependence of the system.

### Site-directed mutagenesis

Nearly every residue in the rhodopsin structure has been examined with site-directed mutagenesis<sup>19,71–73</sup> and new ideas have been generated by the X-ray structure.<sup>74</sup> A variety of experimental methods have been used to assess the behavior of the altered system, focusing mainly on changes in the full photocycle. These results are intriguing for suggesting the possible roles of individual amino acids in the function of the protein. With the presence of the X-ray structure it becomes possible to try and relate this history of mutagenesis to the solved structure and several recent reviews can be consulted for current efforts in this direction.<sup>1,3–8</sup>

## Results

We simulated bovine rhodopsin in the dark-adapted state. For the simulation, the lipid bilayer, salt, and water were represented in atomic detail,

along with the rhodopsin protein and palmitoylated side-chains. Figure 1 shows the outlines of the simulation system. More details are provided in Methods. In the following we concentrate on the analysis and possible implications for rhodopsin function in the 40 ns simulation.

Our results naturally break down into several sub-categories. For easier analysis and reading, we present results in the order: (1) average structure results (validation of the simulation conditions); (2) conditions around the retinal-binding site; (3) large-scale motions (and coupling throughout the system); and (4) lipid and water interactions.

### Average structural results

#### RMS

A measure of the relative stability of a molecular dynamics simulation is the sampling near to the starting point. Since the starting point is a relaxed structure based on the X-ray data, this provides both a measure of the amount of motion seen in the trajectory and the relative deviation from the

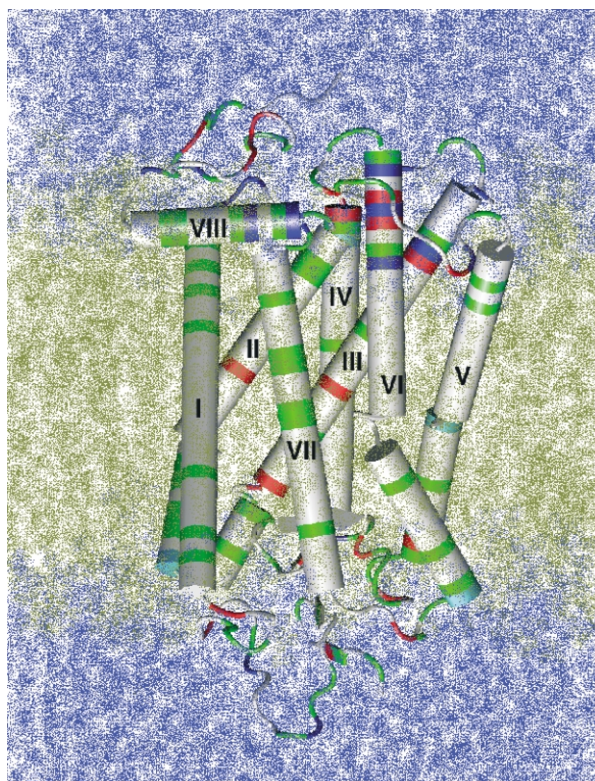


**Figure 1.** Overview of the simulation system used. The water (7441 TIP3) is schematically shown in blue. The lipid (99 DOPC, two palmitate) is shown in tan. This illustrates where the bilayer sits relative to the protein. The protein is illustrated in cartoon form with the helices labeled. Note that the cytoplasmic side is on the top and that helix VIII is the amphipathic helix. The basic residues are colored in the cartoon as blue, the acidic residues are shown in red, the polar residues in green and the non-polar residues in white. The actual simulation was all-atom and all-hydrogen and consisted of 41,623 atoms in total.



experimental starting point. Since simulations cannot, yet, reach long time-scales, a general rule of thumb is that large deviations from the starting point indicate a poorly defined simulation and that analysis of such a simulation would be inappropriate. On the other hand, a well-defined simulation should, at a minimum, have an RMS deviation relative to the starting point that is reasonable. At the same time, the ideal simulation will also have sampled well from the starting point and can comment on the types of motions expected from the static initial point. In Figure 2, we present the average RMS over the 40 ns simulation relative to the simulation starting point. As can be seen clearly, the loops have much more motion than the helices and the average position of the helices stays relatively near to the X-ray starting point. This is especially true in the early stages of the simulation where we did not observe any large changes in the helix orientation or packing. As presented in more detail in this section, later in the simulation, we observe a change in helix tilt and helix kinking that is indicative of a larger scale conformational change. This first figure shows that our simulation is stable and well-defined by current molecular dynamics standards.

Other trends are obvious as well in Figure 2. For example, the largest motions are seen in the C-III and C-terminal regions. This indicates a large amount of relative motion is found in these regions relative to the more restricted motion observed in the helices and the other loop regions. As brought out more in the discussion, this is consistent with experimental information obtained from site-directed spin labeling (SDSL) and NMR.

### B-factors

The recent X-ray structure provides an initial

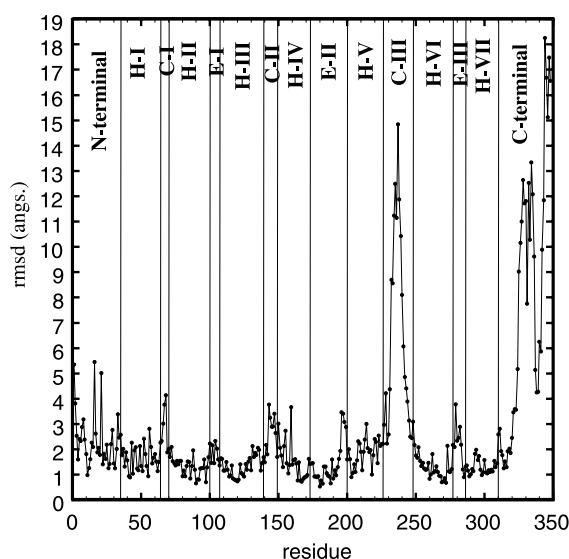


**Figure 2.** RMS of heavy atoms from the X-ray structure during the simulation. Note the larger RMS values for the loops and lower RMS for the helices.

insight into relative motion throughout the rhodopsin protein through Debye–Waller *B*-factors. These assume an isotropic motional model and may thus be biased for certain situations (e.g. if there is more motion in the effective bilayer plane than normal to that plane, then this type of motional model would not be the best for comparison of dynamics). Nonetheless, this comparison is useful, since it provides a rough guide to the types of motion that might be present in the crystal cell used for X-ray analysis and the types of motion that we compute in the lipid bilayer setting. As can be seen in Figure 2, the analysis suggests that there is considerable similarity, in that the loops and termini are more flexible than the interior helical packing regions.

### Retinal binding site

One central mystery for rhodopsin function is the coupling between local changes in the retinal due to light activation and the eventual G-protein amplification mechanisms controlled by G-protein binding changes in the cytoplasmic regions of the GPCR rhodopsin. Even though our simulation time is well short of the full cycle, the molecular dynamics calculations give some insights into the nature of this coupling through analysis of the types of fluctuations seen in the binding site and the amplification and coupling of those changes throughout the full protein molecule. For this type of analysis, we first concentrate on the nature of the average interaction energies, and then comment on the time dynamics of coupling for retinal changes with the local protein environment.

### Dihedral changes

The action of rhodopsin involves the transition of the retinal in the 11-*cis* state to the all-*trans* state. We calculated the dihedral angle for each of the dihedrals in the retinal. Figure 3 shows the dihedral angle as a function of time for several of the retinal dihedrals. The dihedral for the 11-*cis* (C11–C12) is flat, indicating no transition. This is to be expected even for a 40 ns simulation. The time-scale for the transition without the photon adsorption is well beyond the simulation time. However, some of the other dihedrals show transitions. These transitions demonstrate that the retinal molecule is not locked within the rhodopsin such that it cannot move. Furthermore, as these dihedral transitions affect the retinal structure, they affect the interactions between the retinal and the rhodopsin residues. These interactions consequently have many dynamic transitions. We will highlight some of these transitions particularly involving hydrogen bonds in Discussion.

Figure 3 shows that frequent transitions occur for dihedrals about the C<sup>δ</sup>–C<sup>γ</sup> and C<sup>ε</sup>–N16 bonds of Lys296. These dihedral transitions move the relatively highly charged N16, C15 and their hydrogen atoms. These atoms are involved in the

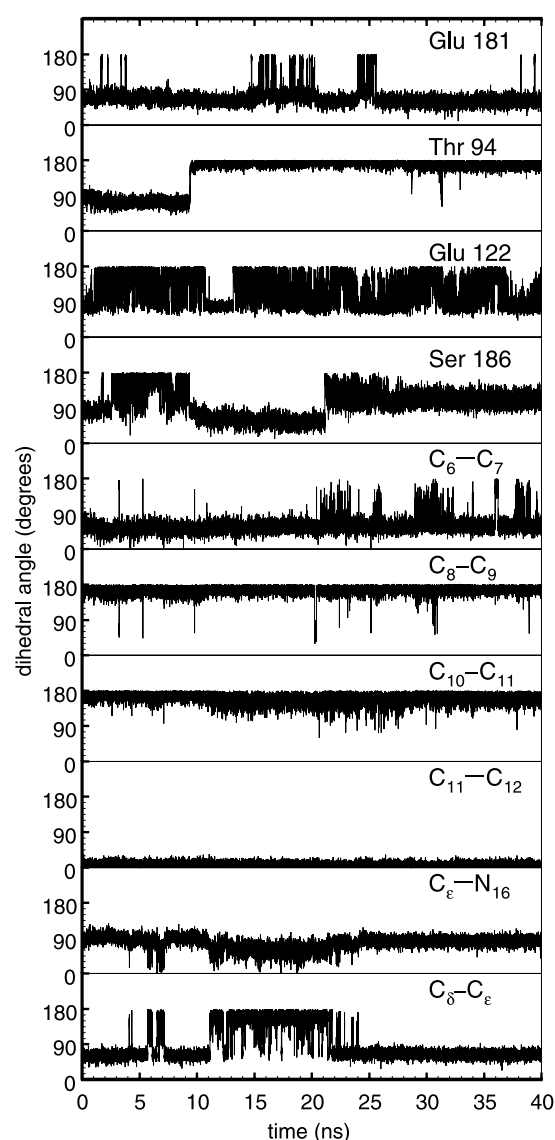


**Figure 3.** Dihedral angle as a function of time for both retinal and nearby side-chains of the protein.

strong interactions with Glu113 in particular (see Figure 5). In addition, the residues Ser186 and Thr94 interact with these atoms, but their energetic transitions (see Figure 6) are more related to their own dihedral dynamics. The dihedral about C10–C11 is very noisy, but does not exhibit many complete transitions. For comparison, the dipoles not shown in Figure 3 do not exhibit transitions and are like the C11–C12 dihedral. There are several short-lived transitions in the dihedral about C8–C9 in the retinal chain. There are numerous transitions particularly for  $t > 20$  ns for the dihedral about C6–C7, which rotates the retinal ring. The position of the retinal ring is consequently frequently varying for  $t > 20$  ns. We see that retinal structure is very dynamic, implying that the interaction state of retinal is also very dynamic. We thus examined the interaction energies between the retinal and nearby rhodopsin residues as a function of time (see below).

The dihedral transitions that occur in nearby side-chains of the protein near the retinal moiety are also illustrated in Figure 3. In particular, note that several transitions occur during the course of the 40 ns trajectory. We find that the transitions near 10 ns reflect changes throughout the protein and possible coupling between the local changes within the binding cavity and the larger scale conformational transitions that could be linked to the M-II state and G-protein signaling mechanisms. For example, Ser186 has three main transitions during the trajectory including one near 10 ns. Glu122 has a series of very rapid transitions separated by a few, short periods of relatively constant dihedral value. Thr94 sees a single large transition near 10 ns and a few rapid fluctuations around 30 ns. Lastly, for illustration of those protein side-chains near where the retinal undergoes conformational changes during the trajectory, Glu181 had four transition periods during the trajectory. This Figure illustrates the importance of having a long trajectory, since these relatively rare transition events may occur only once (e.g. Thr94) during the trajectory.

### Volumetric packing

During the simulation each atom has available to it a range of motions that are primarily restricted by the behavior of the neighboring atoms. Thus, retinal in the binding pocket of rhodopsin is capable of a set of motions that are determined by the interplay between the intrinsic degrees of freedom of the retinal and the environmental restraints provided by the protein itself. Since the cavity is largely protein dominated, there is little role for water and the range of environmental restraints expected from the protein is quite different from what would be expected for retinal in a pure water environment. By computing the range of accessible volumes (Voronoi analysis, see Methods), we compute a set of available spaces that each atom of the retinal is capable of reaching in the simulation. Thus, a larger volume means directly that more motion is possible for that atom type. While this analysis averages the ensemble set of motions into a set of equivalent volumes, it does give an idea of where the largest amount of thermal motion is available to the retinal atoms. In other words, it is hard to directly infer from the size of the cavity the range of forces that lead to that cavity volume, but the range of cavity volumes, across the retinal molecule, give an idea of the range of environmental restraints provided by the protein.

Figure 4 presents a time-averaged picture of available volume for each heavy-atom group of the retinal. The available volume for each atom is calculated using a Voronoi method and averaged over time.<sup>75</sup> Note that the  $x$ -axis moves from the ring atoms (C1 to C6) through the chain atoms (C7 to C16), the methyl groups along the retinal (C17 to C20) and into the main-chain connections (N16

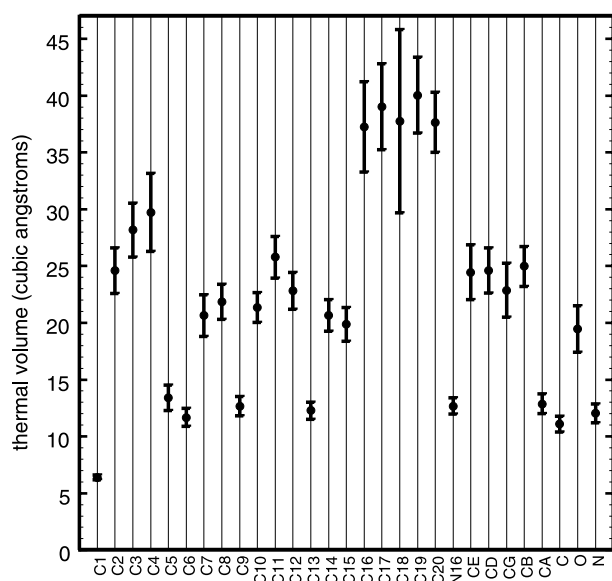


**Figure 4.** Volumetric analysis of the packing in the retinal binding pocket. This reflects a time average using Voronoi analysis of the average space available to each chemical group in the cavity.

to N). In this manner of analysis, the largest free thermal volume is attained by the five methyl groups. The C18 methyl group has the largest fluctuations in the dynamics of the five groups. These large values for the methyl groups are not surprising, since the bond connecting them to the retinal can have relatively strong rates of transition and thus the free volume for each reflects the rotations allowed for the full methyl group. In contrast with the large value seen for the methyl groups, the C1 atom of the ring is nearly an order of magnitude smaller in thermal volume. This implies that this particular heavy atom is much more restricted in relative motion. Again, this can be rationalized, since the C1 atom connects both to the ring atoms (C2 and C6) and to two methyl groups (C17 and C16). Thus, the largest and smallest thermal volumes make sense.

Figure 4 also shows that the ring methylene groups (C2, C3, and C4) have greater thermal volume available to them than doubly bonded chain carbon atoms with one hydrogen. This makes sense as well, since the smaller thermal volumes for chain heavy atoms are for those carbon atoms with methyl groups covalently linked (C9 and C13 to C19 and C20 respectively). Thus, the thermal volumes calculated as averages from the simulation make chemical sense with the size of the groups appended to the carbon driving much of the available free volume.

#### Time-averaged interaction energies

The time-averaged interaction energy  $E_{ave}$  of retinal with the surrounding environment gives insight into the relative importance of different

residue:retinal interactions for functional isomerization. In particular, several experimental groups<sup>1,66,76</sup> have suggested that particular residues (e.g. the Schiff base counter-ion Glu113) are more important than others in the photocycle. In addition, some residues have been suggested to contribute to the coupling between local conformational change and G-protein signaling mechanisms. In this regard, NMR work<sup>60–62</sup> and the X-ray structure<sup>29–31,77</sup> have highlighted residues (e.g. Trp265) that may act as switches in the light-driven conformational change and the connection of protein conformational change to G-protein signaling. While the interaction energies do not directly comment on the possible role of individual amino acids in the switch mechanism, they do provide some guidance as to which amino acid residues are most tightly coupled, energetically, to the retinal. Thus, *a priori*, it is expected that a stronger energetic coupling will imply that changes in retinal conformation (e.g. driven by a light event) will lead to changes in the amino acid side-chain position and conformation. In turn, this may lead to the changes in large-scale protein conformation. As will be presented in the discussion below, energetic transitions due to structural rearrangements are found in our 40 ns simulation. The structural stability of rhodopsin, particularly in relation to retinal, involves many strong interactions that act cooperatively. Thus, this analysis suggests that a single switch mechanism is overly simplified relative to the complex cooperative dynamics that are observed in the simulation.

Interaction energies between retinal and the surrounding residues were computed individually for each surrounding residue interacting with each of three segments of the retinal moiety: the Lys296 residue (bonded to the retinal), the retinal linear chain, and the retinal ring. This enables us to comment on which amino acid residues are interacting with the given regions of the retinal moiety. Figure 5 shows these interaction energies for each part with the nearby residues. Note that we present only those interaction energy terms that are either strongly favorable (less than  $-1$  kcal/mol) or strongly unfavorable (more than  $1$  kcal/mol). The strong interaction energies are typically due to Coulomb interactions (some of which are hydrogen bonds). From the crystal structure,<sup>29,30</sup> there are some expected strong interactions. For example, the terminal N16 of Lys296 is charged and close to the Schiff base counter-ion in Glu113. In addition there is a strong interaction with Glu181. There is another glutamic acid (Glu122) close to the retinal ring. Besides these potential strongly charged interaction sites, there are many possibilities for hydrogen bonds.

With this breakdown we note that only one residue, Glu181, has strong interactions with all three components of the retinal. In this case, it has strong favorable interactions with the chain and the ring, and an unfavorable interaction with Lys296. There is one amino acid, near to the ring,

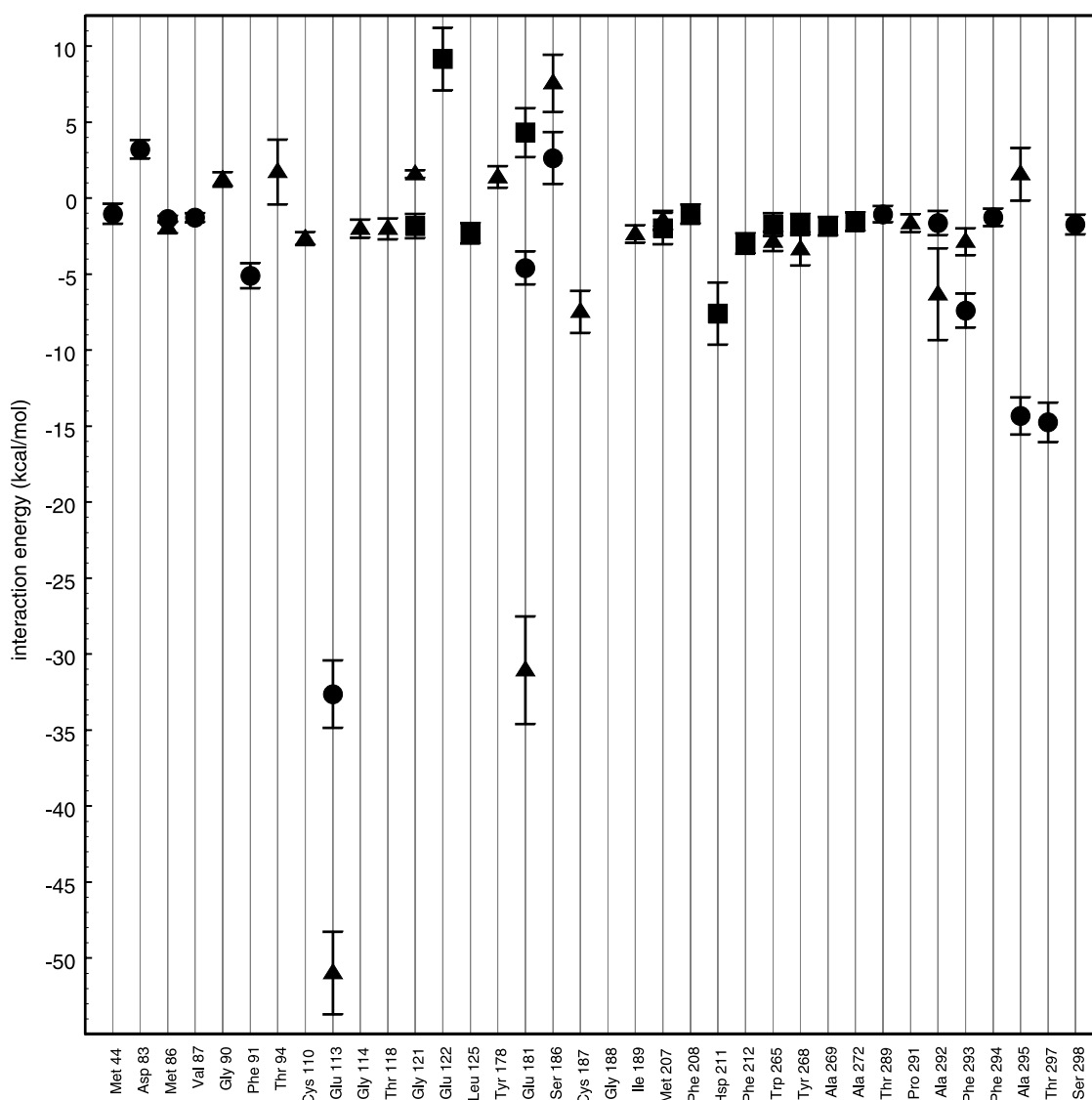


**Figure 5.** Energy of interaction is plotted as a time average. This Figure presents the energetic coupling as a time average between retinal chemical moieties and the surrounding amino acid residues. The retinal ring (squares) is defined as carbon atoms 1, 2, 3, 4, 5, 6, 17, and 18, as well as the associated hydrogen atoms. The retinal chain (triangles) is defined as carbon atoms 7, 8, 9, 10, 11, 12, 13, 14, 15, 19, and 20 and the associated hydrogen atoms. The base (circles) consists of the Lys296 atoms to which the retinal is attached: N16, C $^{\epsilon}$ , C $^{\delta}$ , C $^{\gamma}$ , C $^{\beta}$ , C $^{\alpha}$ , other backbone atoms (C, N, O) and associated hydrogen atoms. For clarity, only interactions with values greater than 1 kcal/mol or less than  $-1$  kcal/mol are shown. Error bars represent standard deviations.

Gly188, which has no strong interactions with the retinal. Given its small size, this amino acid may still play an important role in allowing particular interactions and conformational changes, but it is probably not playing a strong coupling role to the retinal, due to the lack of observed interaction energies.

In a more quantitative analysis, we note from Figure 5 that Glu113 has the most negative average energy of  $-51$  kcal/mol for interaction with the retinal chain and has a  $-32.6$  kcal/mol interaction energy with the main chain of Lys296. In addition, Glu181 shows the second strongest interaction energy with  $-31$  kcal/mol to the retinal chain. Surrounding residues interact with Lys296 mostly *via* its N16 atom, and with the retinal chain mostly

*via* its C15 atom. Both atoms have relatively large partial charges. Besides the Glu residues, three residues close to Lys296 interact strongly with it. Thr297 has an average interaction energy of  $-14.8$  kcal/mol; Ala295 has  $E_{ave} = -14.3$  kcal/mol and Phe293 has  $E_{ave} = -7.4$  kcal/mol. Most of the time average interaction energies for other residues are in the range  $-3$  to  $+3$  kcal/mol. Two other residues have significant attractive  $E_{ave}$  with Lys296 outside this range. They are Phe91 at  $-5.1$  kcal/mol and Glu181 at  $-4.60$  kcal/mol. Residues that interact strongly with the retinal chain are the following. Cys187 has a high average energy of  $-7.5$  kcal/mol. Ala292 has an average energy of  $-6.3$  kcal/mol and Tyr268 has an average energy of  $-3.3$  kcal/mol. In the positive



energy range, only Ser186 with an average energy of +7.5 kcal/mol is outside the most occupied range of interactions with the retinal chain. The strongest interactions with the retinal ring are much weaker than for Lys296 or the retinal tail. Doubly protonated His211 has the most negative average energy of  $-7.6$  kcal/mol and Phe212 is second with  $-3.0$  kcal/mol. There are strong repulsive interactions with the retinal ring, in both cases with Glu residues. The strongest is Glu122 with an average energy of  $+9.1$  kcal/mol, and for Glu181  $E_{\text{ave}}$  equals  $+4.3$  kcal/mol.

#### Time-dependent interaction energies

Changes in interaction energy can provide an idea of how local conformational changes are coupled into larger changes throughout the system. In particular, by looking at the local changes in interaction energy within the retinal-binding pocket, we start to see where changes within this binding pocket might be coupled into larger changes in the helix motions and helix kink angle. While it is difficult to separate cause and effect in a large cooperatively coupled system, looking for events that are correlated in time does give some indication of what change might be related to what other change in the system.

An example of a local interaction energy transition is seen in Figure 6. Part (a) shows the interaction energy between Ser186 and Lys296. A transition with a large energy difference equal to  $-4.7$  kcal/mol occurs at  $t = 9.9$  ns. Initially, the hydroxyl of Ser186 is far from C $^{\epsilon}$  and N16 of Lys296. The transition at  $t = 9.9$  ns is due to a dihedral rotation in Ser186 (see Figure 3) that especially brings the O $^{\gamma}$  close to the oppositely charged C $^{\epsilon}$ . The Figure shows that there were other times in the simulation in which the transition partially occurred (or reversed). Moreover, these transitions are mirrored in the interactions of Ser186 with the retinal chain (Figure 6(b)).

At the same time as the transition at  $t = 9.9$  ns between Ser186 and both Lys296 and the retinal chain, Thr94 has a large transition in its interaction with the retinal chain (Figure 6(c)). Graphical examination of trajectories shows for earlier times, the hydroxyl groups in Thr94 and Ser186 form a hydrogen bond. The energy change indicates the structural rearrangement in which acceptor oxygen changes from the oxygen in Ser186 to the oxygen in Thr94. This brings the Thr94 hydroxyl close to the charged C15 resulting in a large (5.1 kcal/mol) drop in the interaction energy. At about  $t = 21$  ns the Ser186-Thr94 H-bond is broken and a large increase in the energy of the Ser186 occurs, because its hydroxyl moves away from H16 on the retinal. The Thr94 hydroxyl does not change position and its energy remains constant.

The interaction energy for Ala292 with Lys296 (Figure 6(d)) also has a sharp transition in the vicinity of  $t = 10$  ns as well as several up/down transitions of the same magnitude at other times.

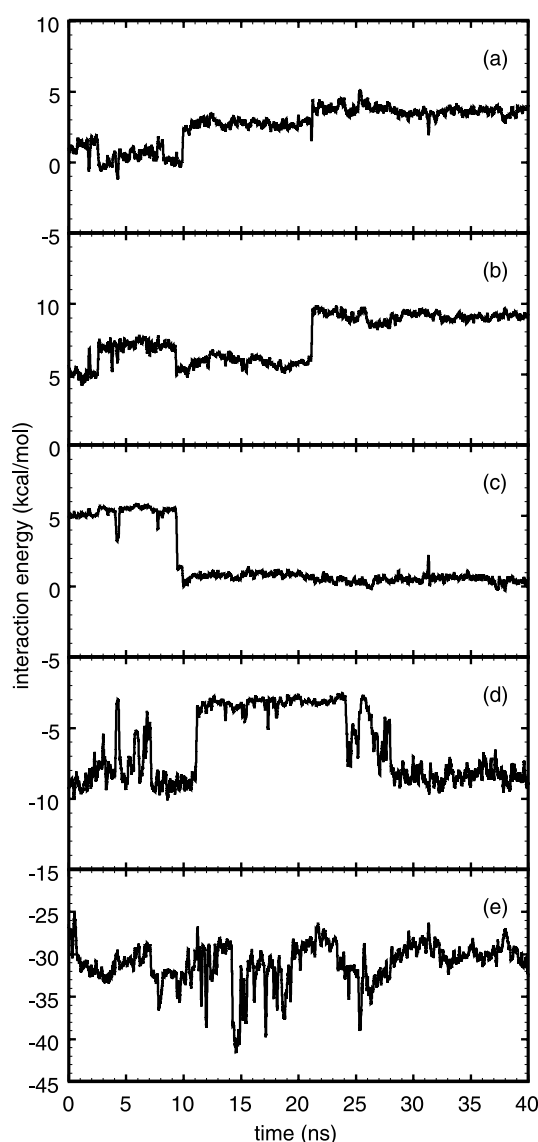


**Figure 6.** Time series of selected residues' interactions with retinal. Interactions are split among Lys296, retinal chain and retinal ring as defined in Figure 5. The time series are for (a) Ser186 interaction with the Lys296; (b) Ser186, (c) Thr94, (d) Ala292 and (e) Glu181 all interacting with the retinal chain. For clarity, the data have been smoothed using a 50-bin boxcar average, which removes the high-frequency fluctuations.

The behavior is indicative of a two-state system. The energy distribution does have two peaks with energies at  $-3.2$  and  $-8.4$  kcal/mol. The source of these strong interactions is the backbone oxygen of Ala292 interacting primarily with the retinal hydrogen H15. As pointed out earlier in the discussion of the dihedral dynamics of the retinal chain (Figure 3), the retinal H15 is affected by dihedral transitions within retinal. These transitions change the separation distance between the Ala292 oxygen and H15, altering the pair's interaction energy.

The retinal dynamics also strongly influences the interaction with the Glu181 residue, which has frequent large transitions as shown in Figure 6(e).

The interaction energy for Glu181 with the retinal chain ranges widely from  $-40$  kcal/mol to  $-25$  kcal/mol. The fluctuations are large, in part because of the strong electrostatic character of the Glu181 interactions. Small changes in distance between Glu181 and retinal yield large energetic variations. The interactions are thus very sensitive to retinal's and its own dihedral dynamics. The distribution has a main peak at  $-31$  kcal/mol with a weak shoulder peak at  $-36$  kcal/mol. One especially large transition occurs at  $t = 14.6$  ns and involves a drop in energy of 11 kcal/mol. This correlates with the beginning of a series of dihedral flips in Glu181 (Figure 3). The dihedral dynamics correlates well with a two-peak interaction energy, since the dihedral angle is predominantly  $65^\circ$ , but spends a minor, but significant fraction of its time at an angle of  $168^\circ$ .

We have calculated the cross-correlation functions between some of the dihedral angles in Figure 3 and the interaction energy of the same residue with retinal in Figure 6. For Thr94 we obtain a correlation coefficient of  $-0.925$ , which shows that almost all of the changes in interaction energy for Thr94 are due to its dihedral dynamics. For Ser186 the correlation coefficient has a smaller, but still large value of 0.59. This implies that some of the interactions involve structural transformations other than the dihedral transitions in Ser186. These transformations could be the dihedral transitions in the retinal molecule or nearby side-chains. The correlation coefficient for Glu181 is  $-0.14$ , a low value. This is not surprising, given that Glu is a charged residue and therefore has a larger interaction range including the entire retinal molecule. Not all of the retinal dihedrals are in sync with the Glu181 dihedral. Thus, not surprisingly, the correlation coefficient is low. These three cases show that when the interaction energy and the structural dynamics are strongly localized the correlation can be very strong. As the interaction range increases, the number of structural transformations within this range that can occur increases. The time correlation is then likely to be small as the events become uncorrelated.

### Summary of section

In summary, for this sub-section, we have identified the interactions that exhibit significant transitions during the simulation. As above for the time-averaged interaction energies, and the dynamic transition energies, retinal was split for analysis into three parts: Lys296, the retinal chain (C7–C15) and the retinal ring (see Figure 5). There are a large number of transitions evident from the time series of these interaction energies. We characterized the structural changes that occur with the energetic transitions. We then highlighted significant interaction sites and the significant transitions that occur during the simulation. We find correlated dynamics. In particular, there are many events that occur near  $t = 10$  ns. These events are

connected to the dynamics of whole helices, which we discuss next.

### Large-scale motions

There is evidence from SDSL (cited above and more in discussion below) that rigid body motion of helix VI relative to helix III could be part of the light-activated photocycle. This type of large-scale rigid body motion is intriguing, at least partly because it may be a common dynamic motion for other hepta-helical receptors. Even bacteriorhodopsin (not a canonical GPCR) has similar rigid body motions. Thus, we wanted to examine our simulation carefully for possible rigid body motions and also wanted to understand, if possible, whether any of the observed rigid body motions could be connected to other changes (e.g. near the retinal-binding site) of rhodopsin.

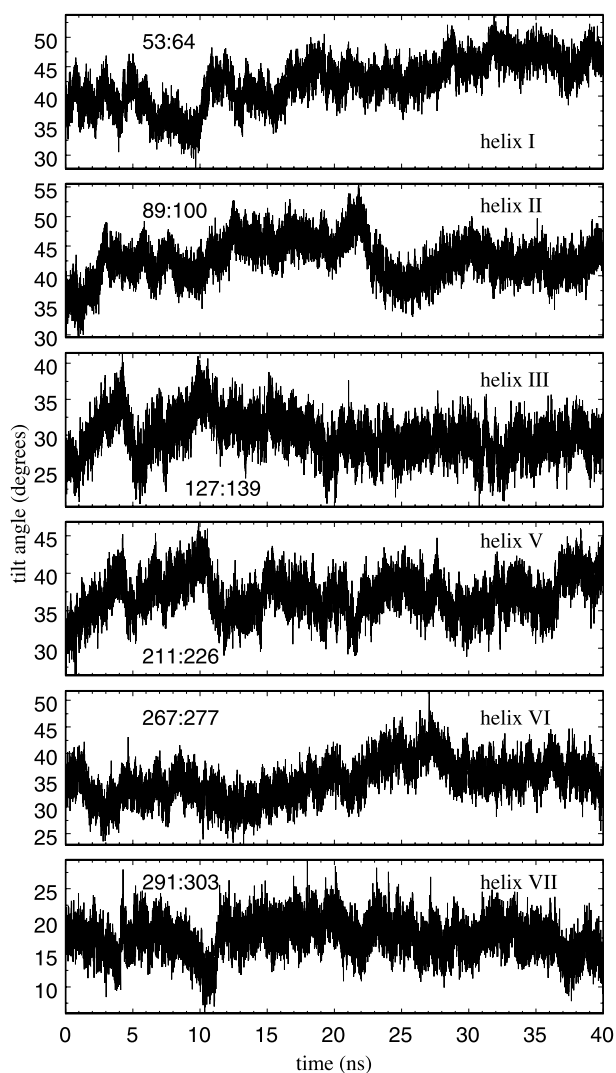


**Figure 7.** Helix tilt angle as a function of time. The tilt angle dynamics shows that large-scale conformational change is present in the 40 ns simulation.

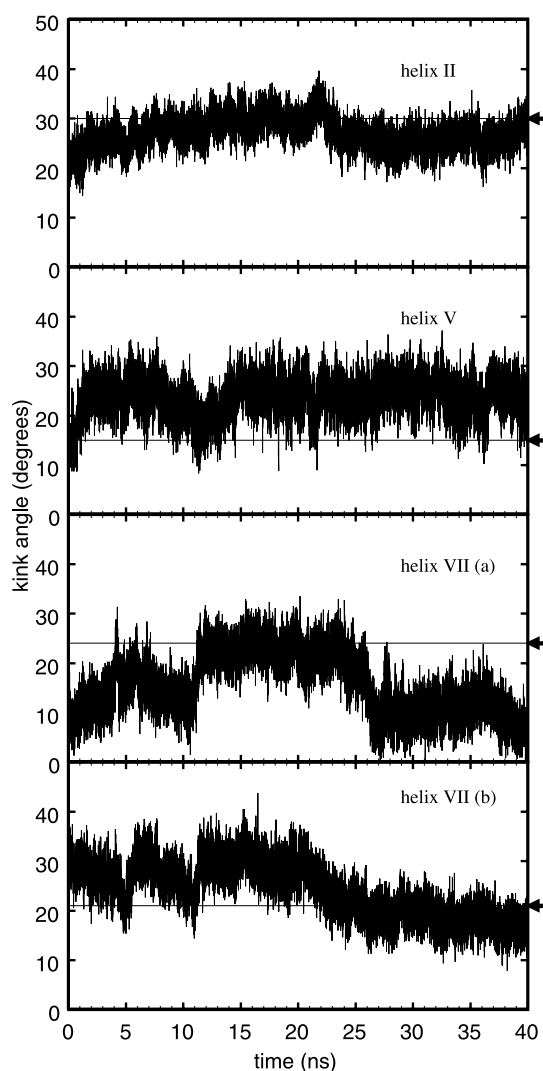
### Changes in helix tilt

Figure 7 shows the tilt angle  $\theta_t$  for some of the seven transmembrane helices over the 40 ns production run time. The tilt angle calculation involves a best-fit cylinder to the helix axis and a calculation of the angle of that cylinder relative to the bilayer normal for each saved conformation of the dynamic trajectory. We have split the helices into sections based on kinks and intrinsic bends. The legend gives the residue ranges used in the calculations. Besides the fast fluctuations of a few degrees, the range between the minimum and maximum tilt angle is about  $15^\circ$  for each helix. As expected, this shows that the seven helix transmembrane protein is not a rigid object, but a dynamical one with various dynamical modes. However, it is expected that the movement induced by the retinal isomerization would be distinct from what is seen here and would be a transition to a different state, with its own fluctuations, rather than a fluctuation within this state.

An examination of the tilt angle data in the vicinity of  $t = 10$  ns shows multiple changes in the tilt angle beyond simple fluctuations. As Figure 7 shows, helices I, II, V and VII have relatively sharp changes in their tilt angles at this time. Helices III and VI exhibit small changes in this period as well. As noted in the discussion of the dynamics of residue interaction energies with retinal, there are several significant transitions that occur in the vicinity of  $t = 10$  ns. The complexity of the multiple helix and individual residue interactions makes deciphering the cause-effect relation intractable. However, the existence of a correlation is strong and clear.

### Changes in helix kink

Changes in helix kink reflect a possible functional role that they may play in rhodopsin protein, similar to, and perhaps greater than, the important role of helix tilt in modulating overall protein conformation and thus G-protein coupling. Three helices, II, V and VII, are known to have significant kinks.<sup>29,30</sup> Figure 8 shows the kink angles  $\theta_k$  as a function of time for the three helices. The kink angles fluctuate within the vicinity of the kink angle found in the X-ray structure. The general characteristics of each helix's  $\theta_k$  are that they vary across a range of about  $20^\circ$  for the 40 ns time period, and that on the picosecond time-scale, fluctuations have about a  $10^\circ$  span. Again we find some significant events occurring in the  $t = 8$ – $12$  ns range. The kink angle centered at Pro291 in helix VII has a sharp transition at about  $t = 11.5$  ns with a reverse transition (less sharp) at  $t = 26$  ns. The kink angle centered at Pro303 in helix VII has narrow dips in  $\theta_k$  at  $t = 5$  and  $11.5$  ns. The kink angle in helix V has a minimum at about  $11.4$  ns. There also is evidence for correlated kink dynamics near  $t = 22$  ns. The kink angle in helix II rises steadily



**Figure 8.** Changes in helix kink angle during the trajectory. The kinks are centered at the following residues: H-II (Gly89); H-V (His211); H-VII(a) (Pro291); and H-VII(b) (Pro303). The lines indicate the kink angle determined from the X-ray structure.

to a maximum at  $t = 22$  ns and then decreases relatively sharply. This maximum occurs at the same time the kink angle centered at Pro303 for helix VII starts a slow decrease. The kink angle data show there is significant large-scale motion on the 40 ns simulation time-scale and that the motion is correlated.

### Changes in helix precession

In addition to asking about changes in helix tilt and helix kink, we can address the amount of precession relative to the bilayer normal that each helix undergoes during the simulation. If a helix were rigidly locked into conformation within the rhodopsin structure, then the helix would see no changes in helix tilt, kink or precession. We computed fluctuations for the precession angle of each helix and again find that there is considerable

motion. The helices had fluctuations of, on average ten degrees on the picosecond time-scale, and typically covered ranges of 50 degrees over the course of the 40 ns simulation. The most nearly perpendicular helix, helix IV, traversed nearly the entire range of precession angles.

### Hydrogen-bonding networks

We believe that changes in hydrogen-bonding networks could be important in the isomerization-driven signaling mechanism. Thus, we provide some insights into the changes of hydrogen bonding between helices during the simulation. Clearly, this type of analysis involves a large amount of data and some arbitrary assumptions about what constitutes a hydrogen-bonding interaction (the CHARMM potential does not use an explicit term for hydrogen bonding). Thus, while the analysis may produce different results with modified assumptions, the relative changes in the hydrogen-bonding networks should be functionally relevant and are thus emphasized.

Analysis of the X-ray structure has led several groups<sup>1,29,30,78</sup> to suggest that certain interactions between helices are important for maintaining the overall structure and may contribute to the dynamics. In particular, they have identified three well-defined networks of hydrogen bonds between helices and an additional fourth possibility. We analyzed the three well-defined networks. Network I is between helices I to II, II to VII, and I to VII (Table 1). Network II involves helix II to helix III and helix II to helix IV (Table 2), and network III involves helices III, V and VI (Table 3).

We computed time averages and dynamic interaction energies for these three networks. Figure 9 shows that hydrogen bond network II has major

**Table 1.** Hydrogen-bonding network as defined by interactions

Site 1	Site 2	$E_{ave}$	SD
OD1, OD2 of Asp83	HD21, HD22 of Asn55	-91.96	5.98
OD1, OD2 of Asp83	HG1 of Ser298	-87.28	6.02
OD1, OD2 of Asp83	HB1, HB2, HB3 of Ala299	-28.18	3.81
O $\ddagger$ of Ala299	HD21, HD22 of Asn55	-12.20	1.24
OE1 of Gln64	HG21, HG22, HG23 of Thr320	-11.99	3.22
OD1 of Asn55	HB1, HB2, HB3 of Ala80	-10.65	1.81
OD1 of Asn55	HB1, HB2, HB3 of Ala299	-4.55	0.77
OD1, OD2 of Asp83	HN of Val300	-18.96	1.42
Tyr43*	Phe293*	42.07	3.13
Tyr43*	Phe294*	42.54	3.11

Hydrogen-bonding network I involves interactions between helices (I,II), (I,VII), (II,VII) and some (I,VIII). Site 1 and 2 denotes the interaction pairs which can be hydrogen bond acceptor/donor pairs, ring:ring cation pi interactions and salt-bridge ion pairs. The default interaction is a hydrogen bond; ring interactions are denoted by \*; backbone interactions by  $\ddagger$ . The site:site interaction energy average ( $E_{ave}$ ) and standard deviation (SD) are given.

**Table 2.** Hydrogen-bonding network number II is defined by interactions between the helices (II,III), (III,IV) and (II,IV)

Site 1	Site 2	$E_{ave}$	SD
OE1, OE2 of Glu113	HG1 of Thr94	-87.57	27.24
OG of Ser127	HD21, HD22 of Asn78	-42.35	9.14
OG1 of Thr160	HD21, HD22 of Asn78	-39.13	10.29
OD1 of Asn78	HE1 of Trp161	-32.23	4.61
OE1, OE2 of Glu113	HG21, HG22, HG23 of Thr94	-20.66	3.04
OE1, OE2 of Glu113	HB of Thr94	-11.01	1.84
O $\ddagger$ of Phe159	HD21, HD22 of Asn78	-7.02	1.55
Trp126*	Met163	61.13	3.93

The default interaction is a hydrogen bond; ring interactions are denoted by \*; backbone interactions by  $\ddagger$ . The site:site interaction energy average ( $E_{ave}$ ) and standard deviation (SD) are given.

energetic transitions at two points in the trajectory. The first major transition is near 10 ns and reflects an increase in the attractive interaction energy from about -100 kcal/mol to about -150 kcal/mol. As we discuss later for Figure 13 this is largely an effect of a change in interaction between Glu113 and Thr94. A second transition and then transition back again occurs near  $t = 20$  ns. In contrast, the hydrogen bond networks I and III showed relatively constant time evolutions with no major transitions like that seen in the second network.

### Lipid and water interactions

There has been discussion in the literature of the possible role of boundary lipids in membrane protein function. The original definition involved a relatively long time-scale for lipid exchange, and is thus clearly not a reasonable way to determine which lipids are boundary lipids for relatively short molecular dynamics calculations. Still, we expect that a boundary lipid can be defined, at least partially, as a lipid that has much higher energetic interactions with the protein than with the other lipids. This definition naturally leads to questions about the details of the interactions between the lipids and the protein. Can we start to rationalize the finding that rhodopsin function

**Table 3.** The hydrogen-bonding network III is defined by interactions between the helices (III,VI), (III,V) and (V,VI)

Site 1	Site 2	$E_{ave}$	SD
Glu247	Arg135	-216.42	10.21
Thr251 (side chain)	Arg135	-171.55	4.54
Glu134	Arg135	-157.92	9.62
OE1, OE2 of Glu122	HD1, HE1, HD2 of His211	-125.89	5.98
OE1, OE2 of Glu122	HD1, HE1, HZ2 of Trp126	-81.51	8.85
Trp126*	His211*	55.23	3.58

Ring interactions are denoted by \*.



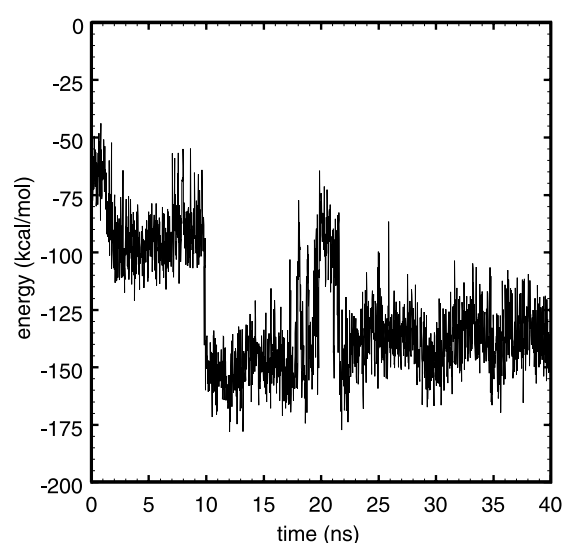


**Figure 9.** Changes in the total energy within the hydrogen bonding network II. Smaller fluctuations were observed in the first and third hydrogen bonding networks.

depends on lipid type? To examine this issue, in Figure 12 we present histograms of lipid interaction energies.

The role of the water and water/lipid transition region in membrane protein function will also be important. We expect that the conformations of the loop, and N and C-terminal tails will be critical for G-protein coupling and will be strongly influenced by their interactions with water. Thus an analysis of the energetic interactions of water with various regions of the protein gives some indications of those regions that are more defined by solution (water) interactions than by membrane (lipid) interactions.

#### Changes in solvent-accessible area

Consideration of the water and lipid-accessible surface areas for each helix and loop region provides further insight into the role of the solvent. By comparing in Table 4 the amount of water-exposed area on each helix, we note that some helices (e.g. helix VII) have little water-exposed surface area, while others (e.g. helices II and III) have a factor of nearly 10 more water-exposed surface area. Similar differences are observed for the lipid-exposed regions. As will be discussed later, we find a transition in solvent-accessible area during the calculation. This could be important for function, since the G-protein coupling may involve changes in water-accessible regions and binding of G-protein to rhodopsin will clearly be dictated by relative accessibility.

#### Solvent interaction energies

Treating each helix as a separate interaction motif, we computed histograms of the interaction

**Table 4.** Accessible surface areas ( $\text{\AA}^2$ )

	Lipid	Water
Helix I	1356 $\pm$ 69	44 $\pm$ 22
Helix II	439 $\pm$ 44	139 $\pm$ 26
Helix III	331 $\pm$ 34	151 $\pm$ 43
Helix IV	840 $\pm$ 45	210 $\pm$ 40
Helix V	931 $\pm$ 56	43 $\pm$ 19
Helix VI	642 $\pm$ 49	132 $\pm$ 45
Helix VII	583 $\pm$ 31	19 $\pm$ 13
Helix VIII	247 $\pm$ 49	157 $\pm$ 78
N-terminal	4 $\pm$ 5	1966 $\pm$ 73
C-I loop	17 $\pm$ 8	351 $\pm$ 57
E-I loop	107 $\pm$ 30	88 $\pm$ 33
C-II loop	108 $\pm$ 39	688 $\pm$ 70
E-II loop	60 $\pm$ 26	649 $\pm$ 63
C-III loop	113 $\pm$ 35	1473 $\pm$ 136
E-III loop	6 $\pm$ 6	318 $\pm$ 54
C-terminal	22 $\pm$ 18	1963 $\pm$ 221

energy between the helix and all of the water, all the lipids or the remaining protein. The results are given in Table 5. In each case, the net protein interaction was stronger than that from the lipid. Interestingly, the interaction with water was stronger than that for protein for some conformations of helix IV during the simulation. Otherwise, for the remaining helices, the interaction from water to helix was less than that for helix to protein interaction. As we compare the range of helix to water and helix to lipid

**Table 5.** Interaction energies for each helix with its surroundings

		Energy (kcal/mol)				
		Self	Protein	Lipid	Water	Total
Helix I	Average	429	-270	-154	-61	-55
	Stdev	17	20	18	17	21
	Max	493	-219	-105	-6	10
	Min	372	-345	-208	-120	-123
Helix II	Average	369	-375	-141	-137	-284
	Stdev	18	23	25	30	23
	Max	431	-301	-64	-55	-200
	Min	304	-450	-222	-244	-349
Helix III	Average	243	-639	-52	-196	-644
	Stdev	18	37	9	30	27
	Max	307	-506	-18	-111	-513
	Min	158	-726	-89	-314	-725
Helix IV	Average	456	-211	-154	-252	-161
	Stdev	19	32	26	42	26
	Max	523	-110	-71	-103	-55
	Min	400	-307	-246	-387	-252
Helix V	Average	486	-304	-146	-170	-134
	Stdev	18	15	23	30	23
	Max	547	-256	-82	-72	-55
	Min	423	-368	-227	-257	-206
Helix VI	Average	430	-430	-188	-209	-397
	Stdev	25	50	40	62	31
	Max	501	-279	-65	-75	-264
	Min	332	-545	-270	-434	-492
Helix VII	Average	542	-454	-74	-54	-40
	Stdev	19	14	17	14	19
	Max	608	-403	-34	-9	44
	Min	489	-508	-112	-93	-102

interactions, we note that helix I had much stronger lipid than water interactions, some helices (III,IV) had stronger water than lipid and some helices (II,V,VI,VII) had nearly equal interactions. Furthermore, the fluctuations in the interaction distributions varied enormously from one helix to another, suggesting a dynamic range of contributions from the environment. For example, helix VII has a narrow and small contribution from both lipid and water. Helix III has a narrow range of lipid interactions energies, but a broad range (centered on  $-200$  kcal/mol) of water interaction energies.

We can get additional insight into the important role of the environment by consideration of selected individual residue interaction energies with the environment. We examined residues that are believed to also have some role in the overall rhodopsin function and not simply those most water or lipid-exposed. The amino acid residues with strongest interaction with water are those in the N-terminal, cytoplasmic, extracellular or loop regions. For example, the glutamine residues 5, 25, and 33 in the N-terminal region have large electrostatic interactions ( $-165$ ,  $-133$ ,  $-149$  kcal/mol on average). In addition, we observe a set of amino acid residues that have strong interactions with the lipid setting. An example is Trp161 with a strong van der Waals (vdW) interaction of  $-7.2$  and Glu201 with an electrostatic interaction of  $-30.3$  kcal/mol. The Glu201 is at the lipid–water interface as one would expect for a strong electrostatic interaction. Lastly, we see particular amino acid residues with especially strong energetic coupling to the rest of the protein. An example of this is Arg135, with  $-270.7$  kcal/mol of electrostatic interaction energy to the protein.

An example of the connection of accessible area and energetics to structure is seen in the C-terminal loop dynamics. Visualization of the C-terminal loop trajectory shows part of the loop appears to bind to helix VIII. Residues 336 to 339 begin to align parallel with helix VIII at  $t \approx 14$  ns and achieve a steady-state structure by  $t = 19$  ns. The interaction energies and the water/lipid-accessible areas for the C-terminal loop change as the structural transformation occurs. Figure 10 shows the energies of the C terminus interacting with the water, lipid, and protein as a function of time. The water energy is the strongest interaction of the three and is attractive. The protein interaction energy is net positive, implying a net repulsion. The mean water interaction increases by about 200 kcal/mol from start to finish. Figure 11 shows that the mean water-accessible area decreases steadily from  $2500 \text{ \AA}^2$  to about  $1700 \text{ \AA}^2$ . Thus, much of the decrease in water interaction energy is due to the depletion of the water around the C terminus and in particular between the C terminus and helix VIII. This is consistent with the binding of part of the C terminus to helix VIII, and the concomitant expelling of intermediate water.

There are more subtle details. Initially, the water

interaction energy is undergoing a cyclic behavior with a 6 ns period (see Figure 10). The kink angle in helix VII (about Pro303), which is next to the C-terminal loop, also undergoes a 6 ns periodic motion in the same time-period (see Figure 8). The end of the third cycle would be at 18 ns, by which time the loop has structurally changed and the water interaction changes too. Thus, we have the kink angle dynamics of helix VII correlated with water interaction energy dynamics of the C-terminal loop, which is restructuring and binding to helix VIII. (Helix VIII connects helix VII and the C-terminal loop.) As we would expect, this example shows that large-scale motion such as helix motion is correlated with the motion and energetic dynamics of neighboring large-scale structures (helices, loops, or tails).

The restructuring of the C-terminal loop is also seen in the interaction energies with the lipids and protein. As the water interaction increases, Figure 10 shows the protein interaction decreases by about 150 kcal/mol. A more favorable interaction has been made as the loop binds to helix VIII. The interaction with the protein is net negative at  $t = 13$  ns when the residues 337–339 are being pulled toward helix VIII. There is a long steady decrease in the protein interaction energy for  $t > 20$  ns. This correlates with increase in water interaction energy and the decrease in lipid interaction energy. At about  $t = 19$  ns a transition appears in the lipid interaction energy. Once the C-terminal loop has formed its new configuration, the lipids appear to reorganize, minimizing their interaction energy. The lipid-accessible area

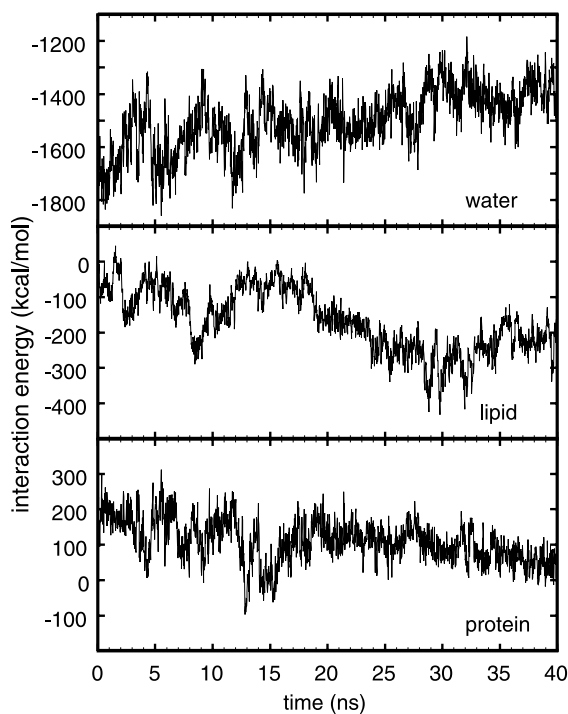


**Figure 10.** Interaction energy as a function of time for the C-terminal loop with the water, lipid and solvent.

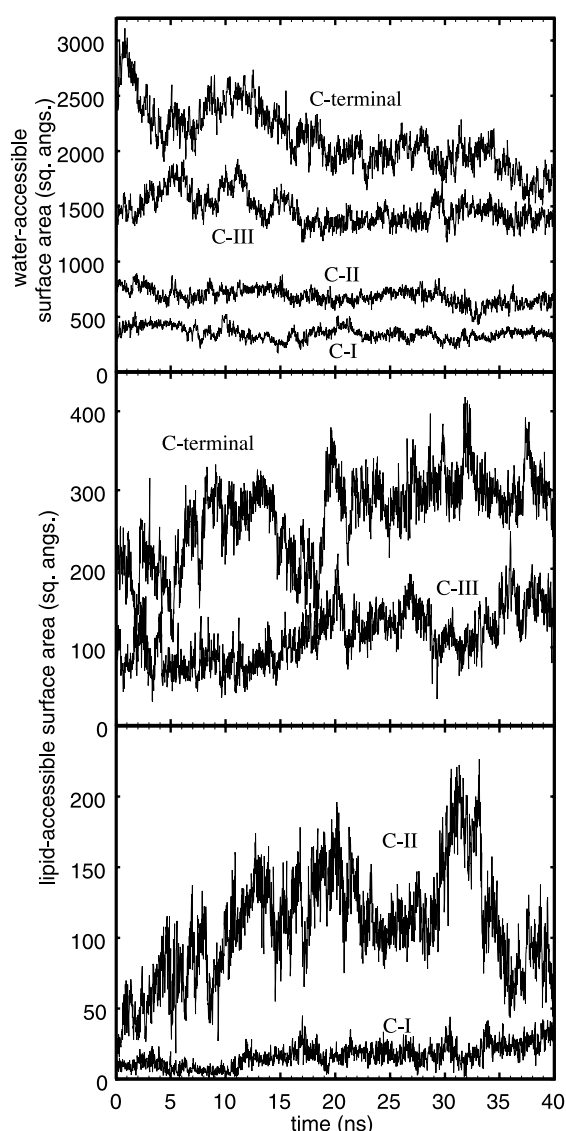


**Figure 11.** Changes in solvent-accessible surface area during the simulation for the C-terminal domain and the cytoplasmic loops: C-I, C-II, and C-III.

increases during the run with a large transition at  $t = 20$  ns coinciding with the energetic change in Figure 10.

We finally note that the C-III loop also shows significant motion, as one might expect for such a long loop. Initially, the loop is bent back down on the outside of the protein, but within 6 ns it moves to being bent away from the protein into the cytosol. The interaction energies with the water, lipid and protein are not as dramatic as for the C-terminal loop, but there is a noticeable drop in the water interaction energy of about 150 kcal/mol occurring in the first 10 ns when the loop is changing its orientation. The protein interaction energy has a maximum at about  $t = 10$  ns. Figure 11 shows that the water-accessible area increases in the first 6 ns when the loop is extending into the water.

## Discussion

The current molecular dynamics calculations provide initial insights into the coupling between local changes in the retinal-binding pocket and larger conformational changes in the whole protein. These larger changes, in turn, should connect into the G-proteins that underlie signal amplification and transduction in this system. Though we do not explicitly analyze the simulations for comparison to other GPCRs, some features may well be common among the rhodopsin system and other GPCRs.

One key finding from the results should be emphasized at this point. That is, much of the rhodopsin literature is filled with site-directed mutations and single pathway schemes that strongly imply that a particular amino acid or a particular defined sequence of events is the underlying key for light-activation of rhodopsin. The current simulations suggest that no single amino-acid dominated view is going to capture the cooperative nature of interactions and transitions within the system. In other words, the collective nature of the motions leads to a stabilization of the dark-adapted state and to a focused ability of the current system to eventually respond to the light activation. We do not explicitly simulate the light-dependent changes and the activation of the G-proteins, but the process of fluctuations in the dark-adapted state are part of the pathway to the light-adapted state. Eventually, this leads through collective motions in response to a light activation, to a functional change.

Further emphasizing this finding of our simulation exploring collective behavior near the dark-adapted state is that we do not see an 11-*cis* isomerization within the simulation. This is consistent with evolutionary pressure to produce a system that responds in exquisite detail to the presence of the light event. That is, we do not expect that the fluctuations within the dark-adapted state will be strong enough energetically to produce a high likelihood of a transition into the light-adapted state. The fact that we do see local transitions that couple into large-scale helix transitions is demonstrative of the types of coupling from a local light adapted change to a larger G-protein signaling that we expect in the full photocycle.

Certainly there is a great wealth of molecular information in the simulations and we cannot present, or even analyze, all possible events. To frame our discussion of the results presented above we have elected to pursue four themes in more detail: (1) the importance of hydrogen bonding and salt-bridge networks; (2) the possible role of lipids in modulating functional behavior; (3) the large changes seen in the cytoplasmic loops and C-terminal region; and (4) the possible coupling of local structural changes to larger scale changes in the protein as seen from this simulation.

### Importance of interaction networks

We analyzed both the local hydrogen-bonding network surrounding the retinal and the network of interactions between helices and between helices and the solvent. At each stage we see some networks that remain strongly coupled throughout the simulation (e.g. hydrogen-bonding network I) and others that dynamically evolve during the trajectory (e.g. hydrogen-bonding network II). As we have already emphasized, the second hydrogen-bonding network (between helices II and III, helices III and IV and II and IV) showed a major transition to a lower energy form (roughly  $-40$  kcal/mol moving to  $-100$  kcal/mol). A major part of this transition was a change in the strength of the hydrogen bond between the oxygen atoms of the Glu113 side-chain (OE1, OE2) and the HG1 of the Thr94 side-chain (the hydroxyl hydrogen). This type of change appears to have been initiated by a change in the local orientation of side-chains around the retinal group that then led to the large change in the hydrogen-bonding network (see Figure 13). As noted in the discussion of tilt angle dynamics, several of the helical sections undergo large changes in tilt angle at this time. Figure 13 shows a blow-up of the increase in the tilt angle of helix I from  $33^\circ$  to  $45^\circ$  within a nanosecond of  $t = 10$  ns. These results further emphasize the cooperative nature of fluctuations and thus dynamics in this system (Table 6).

In addition to hydrogen bonds, salt-bridges are important to interaction networks. The crystal structure<sup>29,30</sup> suggested a strong salt-bridge between residues Glu134 and Arg135, and this was also emphasized in review articles.<sup>1</sup> We computed the interaction energy between this salt-

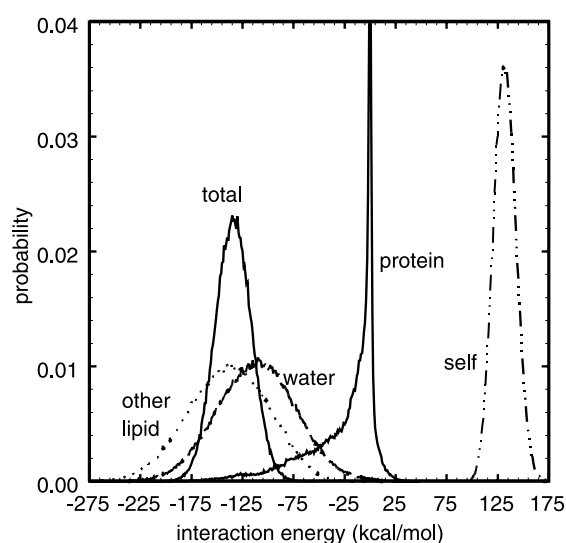


**Figure 12.** Histograms of interaction energies for individual lipid molecules. Shown are the distributions of lipid self-energies as well as interaction energies between individual lipids and the other lipids, water, protein, and the total interaction energy. This suggests the important role of solvent for the system.

bridge and the alternative salt-bridge between Glu247 and Arg135. This latter salt-bridge has been suggested as part of the transition into the M-II state.<sup>1</sup> We find that the Glu247 to Arg135 salt-bridge is much stronger (a factor of roughly 2) than the first bridge. However, both salt-bridges are present energetically throughout the

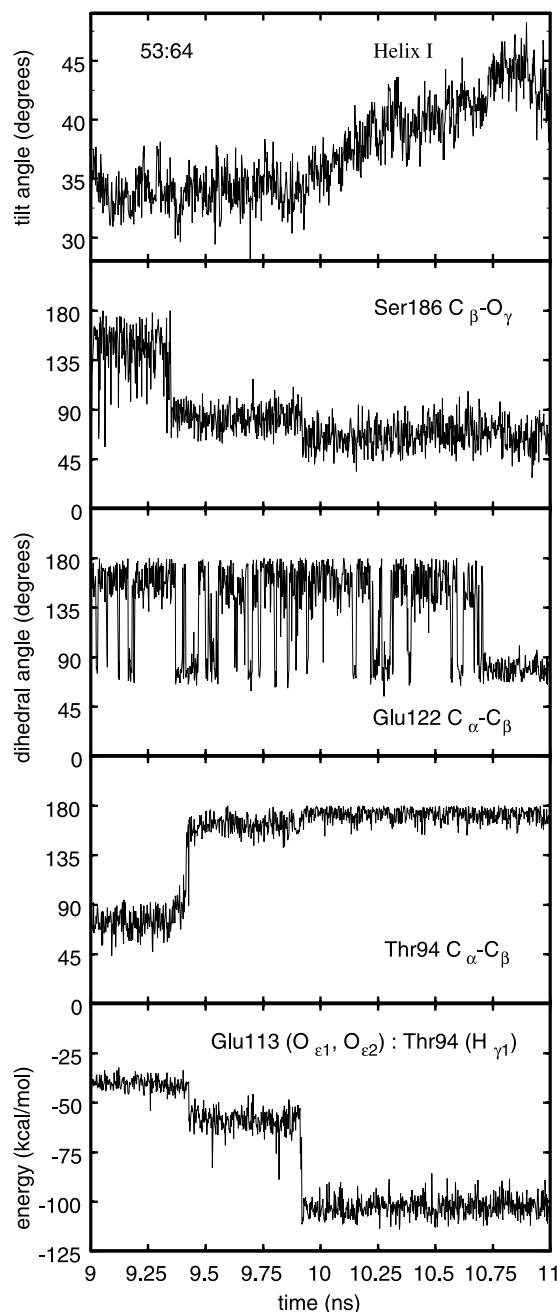


**Figure 13.** Local changes around the retinal binding pocket can lead to larger changes *via* coupled changes in the local binding interactions, changes in the hydrogen-bonding network and then to changes in helix tilt. This Figure shows changes in three dihedral angles of side-chains near the retinal, and the change in interaction energy of the Glu113 interaction with Thr94 (part of the second hydrogen-bonding network). The large change in the tilt angle of helix I is one example of a large-scale motion.



**Table 6.** Energy (kcal/mol) in hydrogen-bonding networks

	Network I	Network II	Network III
Ave	−134.85	−126.15	−298.18
Min	−163.76	−178.14	−337.53
Max	−101.36	−38.89	−241.20
Stdev	9.49	26.99	13.07

dark-adapted rhodopsin simulation. This suggests that the electrostatic coupling in the system is strongly present throughout the protein and that changes in the relative balance of electrostatics may be more revealing than arguments of an all or none nature (i.e. suggesting that a salt-bridge is fully present or fully absent).

### Possible effects of lipids

Both lipid and water play a role in coupling the protein motion and the degree of relative strengths of residue:residue and residue:retinal interactions. We would not expect the same type of dynamics to be observed in a different type of bilayer or in a bilayer mimic. Thus, the solvent (meaning both water and lipid) plays an important role in modulating the types and strengths of interactions that are present in the simulation. The surface tension may have an important effect on the ability of rhodopsin to change conformation and for coupling to occur between G-proteins and the rhodopsin protein. This idea of a coupling between the mesoscopic properties of the lipid bilayer and the transition from dark-adapted to M-II rhodopsin has been tested by the Brown group.<sup>7–11,79</sup> The initial results from our simulation do not directly comment on the mixed lipid systems that Brown *et al.*<sup>7–9</sup> used, but we do find intriguing the types of specific interactions as seen in Figure 12. In particular, a mechanism related to surface tension effects is specific lipid:protein interactions being important in defining the energetic barriers to transition. This is also consistent with experiments.<sup>80,81</sup>

As emphasized in Results, we observed a wide range of helix coupling to the lipid environment. Some of these results are presented in Table 5. These varied from the relatively weak coupling of helix III to the much stronger, and more broadly distributed coupling of helix VI. These two helices are especially intriguing due to suggestions that rigid body motion of these two helices (and/or helix IV) could underlie the M-II transition. Helix VI has been especially strongly singled out as a candidate for rigid body motion. Since simulations show that the coupling to lipid is so broad, this suggests that changes in lipid type (and/or surface tension) could have a broader effect on the M-II transition due to coupling with helix VI than with any other helix. In other words, the distribution of helix:lipid interaction energies is consistent with the experimental observation of a lipid dependence to the M-II transition that is coupled through the types of energetic fluctuations possible between helix VI and the environment.

It is also interesting to note that helix VII (containing the retinal) has a bifurcated distribution for the helix:lipid interaction with maxima at about −60 and −90 kcal/mol. This suggests a type of metastable arrangement to the helix:lipid interactions that could also be important for the M-II transition.

In a similar way to the lipid:helix interaction energies, it is interesting to note that the helix:water interactions show a similar trend; helix VI has the widest distribution of possible energetic interactions. In particular, in some time periods helix VI has the strongest conformational coupling to the water and in other periods it is the third weakest helix for coupling to the water. If the degree of water coupling is varied through lipid type and or through lipid surface tension, then this also could be an important mechanism for the environmental regulation of the M-II transition.

### Motions in C-terminal and cytoplasmic loops

Site-directed, spin-labelling (SDSL) and NMR have both suggested that the C-terminal region is highly mobile on the nanosecond time-scale.<sup>72,82,83</sup> Our simulations confirm this suggestion and further suggest the C-terminal region could undergo large changes in conformational environment that could be important for preparing an effective binding site for the G-protein interaction. This is also consistent with mutagenesis results.<sup>76,84,85</sup>

A recent review by Klein-Seetharaman<sup>6</sup> brings together many aspects of SDSL and NMR analysis for comparison to the X-ray structure. In particular, several SDSL studies have shown large mobility in the C-terminal domain.<sup>56,71</sup> Likewise the cytoplasmic loop between helices V and VI has been studied<sup>86</sup> and similar conclusions drawn about the mobility. The involvement of the C-II and C-III loops in G-protein binding was shown by Acharya *et al.*<sup>87</sup>

The coupling between rigid body motions of the helices and the C-terminal and loop regions is another aspect of the trajectory that we find intriguing. While it is difficult to precisely determine the cause and effect for the large changes in lipid and water-accessible surface areas during the simulation, it is reasonable to suggest that the changes in solvent accessibility are driven by the same rigid body motions of the helices that were first initiated by the local changes in the retinal binding pocket. That is, the changes in accessibility first start to occur at about  $t = 10$  ns. Then as time progresses the changes become more dramatic until about  $t = 20$  ns. Beyond then the lipid accessibility remains relatively constant, while the water accessibility changes only moderately. This is intriguing, because it suggests that changes in the helix tilt (rigid body motion) could drive changes in the local environment of the C-terminal and C-III regions. Since these regions are clearly coupled to G-protein signaling, it then is reasonable to suppose that the fluctuations seen in the trajectory that triggered the transition near 10 ns are similar to the types of changes that occur with *cis-trans* isomerization and

the M-II signaling transition that activates G-proteins. While the G-protein signaling and activation are clearly not part of the current model, these large changes in conformation of cytoplasmic domains that are initiated by changes in other parts of the protein system are very intriguing.

### Coupling local changes to larger conformational changes

The results suggest a set of pathways that together couple the local changes in the retinal environment with larger conformational changes. This is neither the steric switch suggested by NMR experiments nor the local-and-independent-domains view of protein motion. Instead, what the simulations appear to suggest is that the conformations visited are a reflection of relatively tight coupling between multiple regions of the protein (not independent units) and of a range of coupling interactions (i.e. not a single residue that is rigidly moved by a change in the retinal conformation). Another way of phrasing this is that there is a range of motion types and amplitudes throughout the simulation and that coupling occurs both through direct residue:residue and residue:solvent interactions as well as through indirect hydrogen-bonding networks such as we see in the second hydrogen-bonding network.

Relatively recent work with chromophore cross-linking<sup>88,89</sup> suggests a model where isomerization leads to changes in helix IV and helix VI with the retinal coming close to Ala169 in the Meta II state. There are several intriguing implications from the simulations. First, the least strongly interacting helix with other parts of the protein is helix IV. The distribution is bimodal with a second lower peak from about  $-150$  kcal/mol of interaction energy. This may reflect that this helix, the shortest and most nearly vertical, is capable of performing the type of motion suggested in the model. Second, helix VI has a long-tailed distribution from a strong interaction energy towards a much weaker interaction with the rest of the protein. The energy varies from a distribution peak at  $-450$  kcal/mol to a set of weaker interactions around  $-300$  kcal/mol. This distribution is the widest of all the seven helices. It suggests that fluctuations in the helix interaction energy, coupled with the light-driven isomerization change could drive large helix motions, such as suggested in the cited model. Other experimental work<sup>60,90</sup> is also consistent with the thought of rigid body helix motions for the transition to the M-II state.

It is interesting to speculate on the possible structural changes that might underlie the M-II transition from our calculations. The results are consistent with an opening of the cytoplasmic domain and with rigid body motion of the helices. This is especially true for helix VI, where we see broad interaction distributions and evidence of a different class of mobility relative to the other helices. It is possible that the M-II transition

involves changes in the cytoplasmic accessibility, and in the tilt of helix IV, as well as in the tilt of helix III, the most tightly coupled of the helices. Recent work from the Yeagle group<sup>91</sup> is also consistent with these ideas.

A further point of comparison is with the large number of other class A GPCRs. It appears that many of the most conserved residues in these primary sequences have important roles in rhodopsin function. Furthermore, the details of coupling to G-proteins through changes in the cytoplasmic loops and C-terminal region seem to be conserved.<sup>92–97</sup> It will be interesting to see if the regions from the extracellular loops interacting with the retinal chromophore will also be involved with transitions and binding in other GPCRs.<sup>2,98,99</sup>

### Conclusions

This is an exciting time for those interested in GPCRs and G-protein mediated signaling systems. The recent X-ray structure of bovine rhodopsin and the large amount of primary sequence information suggests that we may soon be able to understand the molecular events that drive signal recognition and signal amplification at a molecular level. The current simulations should be viewed as an initial step towards the fuller connection of molecular structures with molecular function through a detailed understanding of the range of motions that are available to the system. While we do not claim to have understood the full details of light-driven isomerization and the coupling of that motion change to eventual signaling and amplification, the simulations do provide an initial view of the types of conformations available to dark-adapted rhodopsin within a lipid bilayer setting. We feel that the calculations elucidate the possible types of coupling seen between local and large-scale protein change that may be important for the light-driven coupling underlying visual function.

### Methods

We aimed to examine the effects of the lipid environment on rhodopsin structure and motion and thus built, from the start, a system to include all-hydrogen, all-atom representations of protein, lipid, and water. For this, it was important to use a consistent force-field that balanced the energies between each of these types of molecules. We elected to work with the CHARMM all-hydrogen force-field (version 22 for protein and version 27 for lipids, both released in August of 1999)<sup>100,101</sup> and used the parameters defined for retinal within the CHARMM force-field.<sup>102</sup> Furthermore, we designed a system that included at least two lipid molecules surrounding the protein in the planar *xy*-directions. Periodic images were used in the *z*-dimension to represent a multilayer system such as studied experimentally by NMR methods.<sup>62</sup> The total system size (41,623 atoms) consisted of protein, 99 DOPC lipids, 100 mM salt concentration (14 sodium, 16 chloride), palmitoylated lipids attached to Cys322 and 323, and 7441 TIP3 water

molecules. All calculations started from the first X-ray structure of rhodopsin (1F88).<sup>29</sup> The CHARMM program was used for the initial construction of the starting point and for the relaxation of the system to a production-ready stage. A modified version of the LAMMPS<sup>103</sup> code using the CHARMM force-field was verified to produce exactly the same energies as the CHARMM code for the initial conformation. Production then occurred at Sandia National Labs taking full advantage of the parallel computation environment provided by the code and the machines. For comparison, a 1 ps simulation takes 312 minutes on the Beowulf cluster at Hopkins using four processors and takes just 2.1 minutes on the Cplant computer at Sandia using 84 processors, or a factor of 150 faster.

### Starting conformation

At the time the simulations were started (August 2000), the only available structure was the 2.8 Å 1F88 structure of the original Science paper.<sup>29</sup> Near the end of the simulation time a second structure (1HZX) with similar resolution (2.8 Å), but an improved R-factor was available from the Rutgers Protein Data Bank.<sup>32</sup> Even more recently, a slightly higher resolution (2.6 Å) structure became available (1L9H).<sup>33</sup> A visual comparison of these structures shows that many of the features of the initial 1F88 structure remain in the other two structures. The changes are more significant with the later (1L9H) structure, where more water molecules are resolved.<sup>33</sup> While we cannot evaluate the effect of the structural changes in starting point on our calculations, we expect that many, if not all, of the general trends reported in this calculation are not strongly dependent on the possible alternative starting points. In the X-ray structure of rhodopsin (1F88) a few regions were not well defined. In particular, we used the CHARMM code to build in the regions of the third cytoplasmic loop (236–239) and the C-terminal tail (328–333) for the starting point of the simulation. In addition, considerable time was spent estimating possible charge states for side-chains in the structure. All solvent-exposed titratable groups were selected in their default ionization state. Less immediately clear is the region surrounding the binding site. Through our initial calculations, we believe that His211, near the binding site should be doubly protonated (+1). This reflects the arrangement of other atoms in the binding site of the 1F88 structure. Similar to a study of rhodopsin in a bilayer mimetic environment, we find that Glu181 is most likely charged.<sup>44</sup> Our charge assignments are at least reasonable, judged by the stability of the structure during the simulation.

### Building the lipid bilayer around the protein

The X-ray structure does not reveal where the lipid bilayer is best placed, nor does it reveal the details of interaction between a lipid bilayer and the protein molecule. We used a method that has been applied in the past to gramicidin and alpha helical systems with success.<sup>104–106</sup> Two ingredients are needed for our method to achieve success. The first is a decision as to the appropriate cell dimensions for the system that we will simulate. This requires a trade-off between the ideals of a very large system that is run for a very long time and the realities of a limited amount of CPU time that scales (roughly) with the square of the number of atoms. We elected to choose a unit cell that has approxi-

mately two layers of lipids surrounding the central protein. This is not an infinitely dilute system where the lipid will reach a bulk (lipid) limit, but at more than 40,000 atoms total, this reflects the largest system that we felt could be built and run with reasonable efficiency. Furthermore, there are arguments that this type of system is that studied experimentally under the concentrations of protein and lipid usually used.<sup>107</sup> A second assumption is the appropriate algorithm for the dynamics. Ideally, a constant normal pressure and constant surface tension approach would be used that adjusts the cell dimensions throughout the simulation to match experimental values. Unfortunately, current molecular dynamics practice has not converged on appropriate methods for constant surface tension or defined the appropriate value for the surface tension in such a simulation. We thus elected to perform the calculation using a constant cross-sectional area with constant normal pressure. This means that the effective (time-averaged) surface tension is determined by the choice of our lateral cell dimensions. Thus, a second ingredient is the optimal choice of cross-sectional area for lipid and rhodopsin molecules. We elected to use the values collected in a recent review of the lipid experimental area (for pure lipid systems)<sup>108</sup> and to estimate the cross-sectional area of rhodopsin using the CHARMM program. This led to a value of 72.2 Å<sup>2</sup> per DOPC molecule and lateral cell dimensions of 55 Å by 77 Å for the total unit cell. Given this starting point, the approach continues with an assumption that the experimentally measured thickness of a DOPC bilayer is near to that adopted for matching to the rhodopsin system. Since experimental work has shown functional activity of rhodopsin in a pure DOPC system, this initial assumption seems reasonable. Then a series of vdW spheres are defined with a rough size near the polar headgroup dimensions of a DOPC. The spheres are placed within the unit cell dimensions of our simulation and are restricted to a planar motion regime. Dynamics is run with the rhodopsin protein fixed and the vdW spheres then adjusting throughout the simulation to pack well within the confines of the rhodopsin protein and the images. After the vdW spheres have defined starting points for lipid headgroups, the lipid bilayer is constructed with sampling of lipid conformations from a pre-defined lipid library containing states representative of the liquid crystalline state. We randomly select lipids from the library and place them with headgroup at the center of a vdW sphere. This creates a starting point with chains, on average, containing the appropriate ratio of *gauche* to *trans* conformations. It also creates a system with a large number of clashes between the alkane chains. To remove this strain on the system, a series of minimizations is then run to slowly relax the alkane chains to a better starting point. After this stage the water is added into the system and the solvent (water and lipid) is then relaxed through a series of minimization and dynamics calculations. In addition to the construction of water and lipid for the system, we elected to add neutralizing salt and excess salt to provide an electrically neutral system that was similar to experimental work for a salt concentration of 100 mM. In addition, after initial equilibration, we converted one DOPC molecule into the two fatty acids covalently linked to the protein through Cys322 and Cys323.<sup>109</sup> Note that a recent molecular dynamics simulation of rhodopsin used a bilayer mimetic rather than explicit lipid as performed here.<sup>44</sup>



### Relaxation to equilibrium state

Starting from a system with lipid molecules, water, salt, and palmitylated protein, we wanted to slowly relax the solvent (lipid and water) to the optimal state, consistent with the X-ray structure of the protein. Clearly there are a number of ways to do this and we describe our approach for this simulation. First we wanted to relax the protein only slowly, so as to let all other degrees of freedom adjust as much as possible before the protein started to move. Towards this end we started with the protein fixed and ran dynamics cycles with electrostatic cutoffs (12 Å) and constant temperature (Nose–Hoover) to relax the solvent. This was performed for 50 ps of dynamics. Then we performed a series of relaxation steps on the system with the protein harmonically restrained to values near to the X-ray starting point. For this step we started at 100 kcal/mol Å<sup>2</sup> and stepped down in steps of 10 kcal/mol Å<sup>2</sup> till the value 50 kcal/mol Å<sup>2</sup> was achieved. This allowed for small adjustments to the protein position to further optimize the solvent starting point. The system was then shifted to constant temperature and pressure with Ewald electrostatics (real space cutoff of 12 Å, sixth order with kappa of 0.320). We started with harmonic restraints on the backbone of 100 kcal/mol Å<sup>2</sup>, for 20 ps, then 50 kcal/mol Å<sup>2</sup> for 20 ps, 25 kcal/mol Å<sup>2</sup> for 20 ps, 5 kcal/mol Å<sup>2</sup> for 10 ps, 2.5 kcal/mol Å<sup>2</sup> for 50 ps, 1.0 kcal/mol Å<sup>2</sup> for 50 ps, 0.5 kcal/mol Å<sup>2</sup> for 50 ps, and 0.1 kcal/mol Å<sup>2</sup> for 50 ps. For these calculations, Nose–Hoover heat-bath coupling was used for constant temperature at 307 K and when used, the pressure was coupled to 1 atm. An additional 250 ps was performed with no restraints on the protein before production ensued.

### Production run and analysis

Initial production was performed with CHARMM on a Beowulf cluster. Performance on the 41,623 atom system was reasonable, but not outstanding. Final production was performed at Sandia National Labs using LAMMPS on a CPlant computer<sup>110</sup> and the performance was roughly two orders of magnitude better. At peak performance (100 processors), throughput of 1 ns/day was achieved. Analysis was performed in CHARMM using the abilities to interrogate trajectories and/or sets of coordinate files.

### Surface area and Voronoi analysis

The accessible area is calculated by use of the CHARMM program where a probe radius is assigned for either a lipid molecule or a water molecule of those regions of the protein that are accessible to a particular type of environmental (solvent) molecule. Voronoi analysis used the C-program routines of Gerstein.<sup>75</sup> In this analysis the hydrogen atoms are ignored and the full effective volume due to the heavy atoms is calculated.

### Acknowledgements

Sandia is a multiprogram laboratory operated by Sandia Corporation, a Lockheed Martin Company, for the United States Department of Energy's National Nuclear Security Administration under

contract DE-AC04-94AL85000. The work at Johns Hopkins was supported under a grant from the American Cancer Society (ACS-RSG-01-048-01-GMC to TBW). L.R.F. was a Royal Society-Fulbright Fellow.

### References

1. Sakmar, T., Menon, S., Marin, E. & Awad, E. (2002). Rhodopsin: insights from recent structural studies. *Annu. Rev. Biophys. Biomol. Struct.* **31**, 443–484.
2. Shi, L. & Javitch, J. (2002). The binding site of aminergic G protein-coupled receptors: the trans-membrane segments and second extracellular loop. *Annu. Rev. Pharmacol.* **42**, 437–467.
3. Filipek, S., Stenkamp, R., Teller, D. & Palczewski, K. (2003). G protein-coupled receptor rhodopsin: a prospectus. *Annu. Rev. Physiol.* **65**, 851–879.
4. Burns, M. & Baylor, D. (2001). Activation, deactivation, and adaptation in vertebrate, photoreceptor cells. *Annu. Rev. Neurosci.* **24**, 779–805.
5. Hubbell, W., Altenbach, C., Hubbell, C. & Khorana, H. (2003). Rhodopsin structure, dynamics, and activation: a perspective from crystallography, site-directed spin labeling, sulfhydryl reactivity, and disulfide cross-linking. *Advan. Protein Chem.* **63**, 243–290.
6. Klein-Seetharaman, J. (2002). Dynamics in rhodopsin. *ChemBiochem*, **3**, 981–986.
7. Gibson, N. & Brown, M. (1993). Lipid headgroup and acyl chain composition modulate the MI–MII equilibrium of rhodopsin in recombinant membranes. *Biochemistry*, **32**, 2438–2454.
8. Brown, M. (1994). Modulation of rhodopsin function by properties of the membrane bilayer. *Chem. Phys. Lipids*, **73**, 159–180.
9. Brown, M. (1997). Influence of nonlamellar-forming lipids on rhodopsin. *Curr. Top. Membr.* **44**, 285–356.
10. Salamon, Z., Wand, Y., Brown, M., MacLeod, H. & Tollin, G. (1994). Conformational-changes in rhodopsin probed by surface-plasmon resonance spectroscopy. *Biochemistry*, **33**, 13706–13711.
11. Wang, Y., Botelho, A., Martinez, G. & Brown, M. (2002). Electrostatic properties of membrane lipids coupled to metarhodopsin II formation in visual transduction journal. *J. Am. Chem. Soc.* **124**, 7690–7701.
12. Botelho, A., Gibson, N., Thurmond, R., Wang, Y. & Brown, M. (2002). Conformational energetics of rhodopsin modulated by nonlamellar-forming lipids. *Biochemistry*, **41**, 6354–6368.
13. Baldwin, B. & Hubbell, W. (1985). Effects of lipid environment on the light-induced conformational-changes of rhodopsin. 2. roles of lipid chain-length, unsaturation, and phase state. *Biochemistry*, **24**, 2633–2639.
14. Litman, B., Kalisky, O. & Ottolenghi, M. (1981). Rhodopsin–phospholipid interactions—dependence of rate of the meta-I to meta-II transition on the level of associated disk phospholipid. *Biochemistry*, **20**, 631–634.
15. Mitchell, D., Niu, S. & Litman, B. (2001). Optimization of receptor-G protein coupling by bilayer lipid composition I—kinetics of rhodopsin-transducin binding. *J. Biol. Chem.* **276**, 42801–42806.
16. Ferretti, L., Karnik, S., Khorana, H., Nassal, M. & Oprian, D. (1986). Total synthesis of a gene for



- bovine rhodopsin. *Proc. Natl Acad. Sci. USA*, **83**, 599–603.
17. Fung, B. & Stryer, L. (1980). Photolyzed rhodopsin catalyzes the exchange of GTP for bound GDP in retinal rod outer segments. *Proc. Natl Acad. Sci. USA*, **77**, 2500–2504.
  18. Sakmar, T., Franke, R. & Khorana, H. (1989). Glutamic acid-113 serves as the retinylidene Schiff-base counterion in bovine rhodopsin. *Proc. Natl Acad. Sci. USA*, **86**, 8309–8313.
  19. Franke, R., König, B., Sakmar, T., Khorana, H. & Hofmann, K. (1990). Rhodopsin mutants that bind but fail to activate transducin. *Science*, **250**, 123–125.
  20. Rao, V. & Oprian, D. (1996). Activating mutations of rhodopsin and other G-protein-coupled receptors. *Annu. Rev. Biophys. Biomol. Struct.* **25**, 287–314.
  21. Zhukovsky, E. & Oprian, D. (1989). Effect of carboxylic-acid side-chains on the absorption maximum of visual pigments. *Science*, **246**, 928–930.
  22. Yokoyama, S. (2002). Molecular evolution of color vision in vertebrates. *Gene*, **300**, 69–78.
  23. Kuwayama, S., Imai, H., Hirano, T., Terakita, A. & Shichida, Y. (2002). Conserved proline residue at position 189 in cone visual pigments as a determinant of molecular properties different from rhodopsins. *Biochemistry*, **41**, 15245–15252.
  24. Noel, J., Hamm, H. & Sigler, P. (1993). The 2.2 Å crystal structure of transducin- $\alpha$  complexed with GTP  $\gamma$  S. *Nature*, **366**, 654–663.
  25. Lambright, D., Noel, J., Hamm, H. & Sigler, P. (1994). Structural determinants for activation of the  $\alpha$ -subunit of a heterotrimeric G-protein. *Nature*, **369**, 621–628.
  26. Hargrave, P., McDowell, J., Curtis, D., Wang, J., Juszczak, E., Fong, S. *et al.* (1983). The structure of bovine rhodopsin. *Biophys. Struct. Mech.* **9**, 235–244.
  27. Unger, V., Hargrave, P., Baldwin, J. & Schertler, G. (1997). Arrangement of rhodopsin transmembrane  $\alpha$ -helices. *Nature*, **389**, 203–206.
  28. Baldwin, J., Schertler, G. & Unger, V. (1997). An  $\alpha$ -carbon template for the transmembrane helices in the rhodopsin family of G-protein-coupled receptors. *J. Mol. Biol.* **272**, 144–164.
  29. Palczewski, K., Kumasaka, T., Hori, T., Behnke, C. A., Motoshima, H., Fox, B. A. *et al.* (2000). Crystal structure of rhodopsin: a G-protein-coupled receptor. *Science*, **289**, 739–745.
  30. Okada, T. & Palczewski, K. (2001). Crystal structure of rhodopsin: implications for vision and beyond. *Curr. Opin. Struct. Biol.* **11**, 420–426.
  31. Stenkamp, R. & Palczewski, D. T. K. (2002). Crystal structure of rhodopsin: a G-protein-coupled receptor. *ChemBiochem*, **3**, 963–967.
  32. Teller, D., Okada, T., Behnke, C., Palczewski, K. & Stenkamp, R. (2001). Advances in determination of a high-resolution three-dimensional structure of rhodopsin, a model of G-protein-coupled receptors (GPCRs). *Biochemistry*, **40**, 7761–7772.
  33. Okada, T., Fujiyoshi, Y., Silow, M., Navarro, J., Landau, E. & Shichida, Y. (2002). Functional role of internal water molecules in rhodopsin revealed by X-ray crystallography. *Proc. Natl Acad. Sci. USA*, **99**, 5982–5987.
  34. Archer, E., Maigret, B., Escrieux, C., Pradayrol, L. & Fourmy, D. (2003). Rhodopsin crystal: new template yielding realistic models of G-protein-coupled receptors? *Trends Pharmacol. Sci.* **24**, 36–40.
  35. Liang, J. (2002). Experimental and computational studies of determinants of membrane–protein folding. *Curr. Opin. Chem. Biol.* **6**, 878–884.
  36. Chamberlain, A., Faham, S., Yohannan, S. & Bowie, J. (2003). Construction of helix-bundle membrane proteins. *Advan. Protein Chem.* **63**, 19–46.
  37. Pan, D., Ganim, Z., Kim, J., Verhoeven, M., Lugtenburg, J. & Mathies, R. (2002). Time-resolved resonance Raman analysis of chromophore structural changes in the formation and decay of rhodopsin's BSI intermediate. *J. Am. Chem. Soc.* **124**, 4857–4864.
  38. Deng, H., Huang, L., Groesbeek, M., Lugtenburg, J. & Callender, R. (1994). Vibrational analysis of a retinal protonated Schiff-base analog. *J. Phys. Chem.* **98**, 4776–4779.
  39. Yan, M., Rothberg, L. & Callender, R. (2001). Femto-second dynamics of rhodopsin photochemistry probed by a double pump spectroscopic approach. *J. Phys. Chem. ser. B*, **105**, 856–859.
  40. Vogel, R. & Siebert, F. (2001). Conformations of the active and inactive states of opsin. *J. Biol. Chem.* **276**, 38487–38493.
  41. Vogel, R. & Siebert, F. (2003). Fourier transform IR spectroscopy study for new insights into molecular properties and activation mechanisms of visual pigment rhodopsin. *Biopolymers*, **72**, 133–148.
  42. Cooper, A. (1979). Energy uptake in the 1st step of visual excitation. *Nature*, **282**, 531–533.
  43. Honig, B., Ebrey, T., Callender, R., Dinur, U. & Ottolenghi, M. (1979). Photoisomerization, energy-storage, and charge separation—model for light energy transduction in visual pigments and bacteriorhodopsin. *Proc. Natl Acad. Sci. USA*, **76**, 2503–2507.
  44. Rohrig, U., Guidoni, L. & Rothlisberger, U. (2002). Early steps of the intramolecular signal transduction in rhodopsin explored by molecular dynamics simulations. *Biochemistry*, **41**, 10799–10809.
  45. Saam, J., Tajkhorshid, E., Hayashi, S. & Schulten, K. (2002). Molecular dynamics investigation of primary photoinduced events in the activation of rhodopsin. *Biophys. J.* **83**, 3097–3112.
  46. Yamamoto, S., Wasada, H., Kakitani, T. & T. Y. (1999). *Ab initio* MO study on the potential energy surfaces for twisting around the C-11=C-12 bond of the protonated Schiff base of retinal. *J. Mol. Struct. (Theochem)*, **461**, 463–471.
  47. Yamada, A., Kakitani, T., Yamamoto, S. & Yamato, T. (2002). A computational study on the stability of the protonated Schiff base of retinal in rhodopsin. *Chem. Phys. Letters*, **366**, 670–675.
  48. Ishiguro, M., Hirano, T. & Oyama, Y. (2003). Modeling of photointermediates suggests a mechanism of the flip of the beta-ionone moiety of the retinylidene chromophore in the rhodopsin photocascade. *ChemBiochem*, **4**, 228–231.
  49. Degrip, W., Liu, R., Ramamurthy, V. & Asato, A. (1976). Rhodopsin analogs from highly hindered 7-*cis* isomers of retinal. *Nature*, **262**, 416–418.
  50. Lewis, J., Fan, G., Sheves, M., Szundi, I. & Kliger, D. (2001). Steric barrier to bathorhodopsin decay in 5-demethyl and mesityl analogues of rhodopsin. *J. Am. Chem. Soc.* **123**, 10024–10029.
  51. Blomgren, F. & S. L. (2002). Using 1,3-butadiene and 1,3,5-hexatriene to model the *cis*–*trans* isomerization of retinal, the chromophore in the visual pigment rhodopsin. *Int. J. Quantum Chem.* **90**, 1536–1546.
  52. Kuksa, V., Franz, B., Maeda, T., Jang, G., Ritter, E.,

- Heck, M. *et al.* (2002). Biochemical and physiological properties of rhodopsin regenerated with 11-*cis*-6-ring- and 7-ring-retinals. *J. Biol. Chem.* **277**, 42315–42324.
53. Sugihara, M., Buss, V., Entel, P., Elstner, M. & Frauenheim, T. (2002). 11-*cis*-Retinal protonated Schiff base: influence of the protein environment on the geometry of the rhodopsin chromophore. *Biochemistry*, **41**, 15259–15266.
54. Farahbakhsh, Z., Hideg, K. & Hubbell, W. (1993). Photoactivated conformational-changes in rhodopsin—a time-resolved spin-label study. *Science*, **262**, 1416–1419.
55. Hubbell, W., Cafiso, D. & Altenbach, C. (2000). Identifying conformational changes with site-directed spin labeling. *Nature Struct. Biol.* **7**, 735–739.
56. Langen, R., Cai, K., Altenbach, C., Khorana, H. & Hubbell, W. (1999). Structural features of the C-terminal domain of bovine rhodopsin: a site directed spin-labeling study. *Biochemistry*, **38**, 7918–7924.
57. Farrens, D., Altenbach, C., Yang, K., Hubbell, W. & Khorana, H. (1996). Requirement of rigid-body motion of transmembrane helices for light activation of rhodopsin. *Science*, **274**, 768–770.
58. Klein-Seetharaman, J., Hwa, J., Cai, K., Altenbach, C., Hubbell, W. & Khorana, H. (2001). Probing the dark state tertiary structure in the cytoplasmic domain of rhodopsin: proximities between amino acids deduced from spontaneous disulfide bond formation between cys316 and engineered cysteines in cytoplasmic loop 1. *Biochemistry*, **40**, 12472–12478.
59. Eilers, M., Ying, W. W., Reeves, P. J., Khorana, H. G. & Smith, S. O. (2002). Magic angle spinning nuclear magnetic resonance of isotopically labeled rhodopsin. *Method Enzymol.* **343**, 212–222.
60. Han, M., Smith, S. & Sakmar, T. (1998). Constitutive activation of opsin by mutation of methionine 257 on transmembrane helix 6. *Biochemistry*, **37**, 8253–8261.
61. Han, M., Groesbeek, M., Smith, S. O. & Sakmar, T. P. (1998). Role of the C-9 methyl group in rhodopsin activation: characterization of mutant opsins with the artificial chromophore 11-*cis*-9-demethylretinal. *Biochemistry*, **37**, 538–545.
62. Han, M., Groesbeek, M., Sakmar, T. P. & Smith, S. O. (1997). The C9 methyl group of retinal interacts with glycine-121 in rhodopsin. *Proc. Natl Acad. Sci. USA*, **94**, 13442–13447.
63. Han, M. & Smith, S. (1997). NMR constraints on the location of the retinal chromophore in rhodopsin and bathorhodopsin. *Biochemistry*, **36**, 7280–7280.
64. Han, M., Lin, S. W., Smith, S. O. & Sakmar, T. P. (1996). The effects of amino acid replacements of glycine 121 on transmembrane helix 3 of rhodopsin. *J. Biol. Chem.* **271**, 32330–32336.
65. Han, M., Lin, S. W., Minkova, M., Smith, S. O. & Sakmar, T. P. (1996). Functional interaction of transmembrane helices 3 and 6 in rhodopsin—replacement of phenylalanine 261 by alanine causes reversion of phenotype of a glycine 121 replacement mutant. *J. Biol. Chem.* **271**, 32337–32342.
66. Han, M. & Smith, S. (1995). High-resolution structural studies of the retinal-Glu113 interaction in rhodopsin. *Biophys. Chem.* **56**, 23–29.
67. Han, M. & Smith, S. (1995). NMR constraints on the location of the retinal chromophore in rhodopsin and bathorhodopsin. *Biochemistry*, **34**, 1425–1432.
68. Shieh, T., Han, M., Sakmar, T. P. & Smith, S. O. (1997). The steric trigger in rhodopsin activation. *J. Mol. Biol.* **269**, 373–384.
69. Smith, S. O., Aschheim, K. & Groesbeek, M. (1996). Magic angle spinning NMR spectroscopy of membrane proteins. *Quart. Rev. Biophys.* **29**, 395–449.
70. Spooner, P., Sharples, J., Verhoeven, M., Lugtenburg, J., Glaubitz, C. & Watts, A. (2002). Relative orientation between the beta-ionone ring and the polyene chain for the chromophore of rhodopsin in native membranes. *Biochemistry*, **41**, 7549–7555.
71. Cai, K., Langen, R., Hubbell, W. & Khorana, H. (1997). Structure and function in rhodopsin: topology of the C-terminal polypeptide chain in relation to the cytoplasmic loops. *Proc. Natl Acad. Sci. USA*, **94**, 14267–14272.
72. Cai, K., Klein-Seetharaman, J., Farrens, D., Zhang, D., Altenbach, C., Hubbell, W. & Khorana, H. (1999). Single-cysteine substitution mutants at amino acid positions 306–321 in rhodopsin, the sequence between the cytoplasmic end of helix VII and the palmitoylation sites: sulfhydryl reactivity and transducin activation reveal a tertiary structure. *Biochemistry*, **38**, 7925–7930.
73. Kim, J., Altenbach, C., Thurmond, R., Khorana, H. & Hubbell, W. (1997). Structure and function in rhodopsin: rhodopsin mutants with a neutral amino acid at e134 have a partially activated conformation in the dark state. *Proc. Natl Acad. Sci. USA*, **94**, 14273–14278.
74. Janz, J., Fay, J. & Farrens, D. (2003). Stability of dark state rhodopsin is mediated by a conserved ion pair in intradiscal loop e-2. *J. Biol. Chem.* **278**, 16982–16991.
75. Gerstein, M., Tsai, J. & Levitt, M. (1995). The volume of atoms on the protein surface: calculated from simulation, using voronoi polyhedra. *J. Mol. Biol.* **249**, 955–966.
76. Arnis, S., Fahmy, K., Hofmann, K. & Sakmar, T. (1994). A conserved carboxylic acid group mediates light-dependent protein uptake and signaling by rhodopsin. *J. Biol. Chem.* **269**, 23870–23881.
77. Bourne, H. & Meng, E. (2000). Rhodopsin sees the light. *Science*, **111**, 733.
78. Sakmar, T. (2002). Structure of rhodopsin and the superfamily of seven-helical receptors: the same and not the same. *Curr. Opin. Cell Biol.* **14**, 189–195.
79. Wiedmann, T., Pates, R., Beach, J., Salmon, A. & Brown, M. (1988). Lipid protein interactions mediate the photochemical function of rhodopsin. *Biochemistry*, **27**, 6469–6474.
80. Beck, M., Siebert, F. & Sakmar, T. (1998). Evidence for the specific interaction of a lipid molecule with rhodopsin which is altered in the transition to the active state metarhodopsin II. *FEBS Letters*, **436**, 304–308.
81. Krishna, A., Menon, S. & Sakmar, T. T. T. (2002). Evidence that helix 8 of rhodopsin acts as a membrane-dependent conformational switch. *Biochemistry*, **41**, 8298–8309.
82. Altenbach, C., Klein-Seetharaman, J., Cai, K., Khorana, H. & Hubbell, W. (2001). Structure and function in rhodopsin: mapping light-dependent changes in distance between residue 316 in helix 8 and residues in the sequence 60–75, covering the cytoplasmic end of helices TM1 and TM2 and their connection loop CL1. *Biochemistry*, **40**, 15493–15500.
83. Altenbach, C., Cai, K., Khorana, H. & Hubbell, W. (1999). Structural features and light-dependent changes in the sequence 306–322 extending from

- helix VII to the palmitoylation sites in rhodopsin: a site-directed spin-labeling study. *Biochemistry*, **38**, 7931–7937.
84. Anukanth, A. & Khorana, H. (1994). Structure and function in rhodopsin. requirements of a specific structure for the intradiscal domain. *J. Biol. Chem.* **269**, 19738–19744.
  85. Mielke, T., Alexiev, U., Glasel, M., Otto, H. & Heyn, M. (2002). Light-induced changes in the structure and accessibility of the cytoplasmic loops of rhodopsin in the activated M-II state. *Biochemistry*, **41**, 7875–7884.
  86. Altenbach, C., Yang, K., Farrens, D., Farahbakhsh, Z., Khorana, H. & Hubbell, W. (1996). Structural features and light-dependent changes in the cytoplasmic interhelical E-F loop region of rhodopsin: a site-directed spin labeling study. *Biochemistry*, **35**, 12470–12478.
  87. Acharya, S., Saad, Y. & Karnik, S. (1997). Transducin- $\alpha$ -C-terminal peptide binding site consists of C-D and E-F loops of rhodopsin. *J. Biol. Chem.* **272**, 6519–6524.
  88. Borhan, B., Souto, M., Imai, H., Shichida, Y. & Nakanishi, K. (2000). Movement of retinal along the visual transduction path. *Science*, **288**, 2209–2212.
  89. Meng, E. & Bourne, H. (2001). Receptor activation: what does the rhodopsin structure tell us? *Trends Pharmacol. Sci.* **22**, 587–593.
  90. Beck, M., Sakmar, T. & Siebert, F. (1998). Spectroscopic evidence for interaction between transmembrane helices 3 and 5 in rhodopsin. *Biochemistry*, **37**, 7630–7639.
  91. Choi, B., Landin, J., Galan, J., Birge, R., Albert, A. & Yeagle, P. (2002). Structural studies of meta-rhodopsin II, the activated form of the G-protein coupled receptor, rhodopsin. *Biochemistry*, **41**, 7318–7324.
  92. Chung, D., Zuiderweg, E., Fowler, C., Soyer, O., Mosberg, H. & Neubig, R. (2002). NMR structure of the second intracellular loop of the  $\alpha$ 2a adrenergic receptor: evidence for a novel cytoplasmic helix. *Biochemistry*, **41**, 3596–3604.
  93. Dastmalchi, S., Kobus, F., Iismaa, T., Morris, M. & Church, W. (2002). Comparison of the transmembrane helices of bovine rhodopsin in the crystal structure and the C- $\alpha$  template based on cryo-electron microscopy maps and sequence analysis of the G protein-coupled receptors. *Mol. Simul.* **28**, 845–851.
  94. Davies, A., Gowen, B., Krebs, A., Schertler, G. & Saibil, H. (2001). Three-dimensional structure of an invertebrate rhodopsin and basis for ordered alignment in the photoreceptor membrane. *J. Mol. Biol.* **314**, 455–463.
  95. Greasley, P., Fanelli, F., Scheer, A., Abuin, L., Nenniger-Tosato, M., DeBenedetti, P. & Cotecchia, S. (2001). Mutational and computational analysis of the  $\alpha$ (1b)-adrenergic receptor. involvement of basic and hydrophobic residues in receptor activation and G protein coupling. *J. Biol. Chem.* **276**, 46485–46494.
  96. Lu, Z., Saldanha, J. & Hulme, E. (2002). Seven-transmembrane receptors: crystals clarify. *Trends Pharmacol. Sci.* **23**, 140–146.
  97. Terakita, A., Yamashita, T., Nimbari, N., Kojima, D. & Shichida, Y. (2002). Functional interaction between bovine rhodopsin and G protein transducin. *J. Biol. Chem.* **277**, 40–46.
  98. Petry, R., Craik, D., Haaime, G., Fromme, B., Klump, H., Kiefer, W. *et al.* (2002). Secondary structure of the third extracellular loop responsible for ligand selectivity of a mammalian gonadotropin-releasing hormone receptor. *J. Med. Chem.* **45**, 1026–1034.
  99. Prioleau, C., Visiers, I., Ebersole, B., Weinstein, H. & Sealfon, S. (2002). Conserved helix 7 tyrosine acts as a multistate conformational switch in the 5HT<sub>2C</sub> receptor—identification of a novel “locked-on” phenotype and double revertant mutations. *J. Biol. Chem.* **277**, 36577–36584.
  100. Schlenkerich, M., Brickmann, J., MacKerell, A. D. J. & Karplus, M. (1996). An empirical potential energy function for phospholipids: criteria for parameter optimization and applications. In *Biological Membranes: A Molecular Perspective from Computation and Experiment* (Merz, K. M. Jr & Roux, B., eds), pp. 31–81, Birkhauser Press, Boston, MA.
  101. MacKerell, A., Bashford, D., Bellott, M., Dunbrack, R., Evanseck, J., Field, M. *et al.* (1998). All-atom empirical potential for molecular modeling and dynamics studies of proteins. *J. Phys. Chem. ser. B*, **102**, 3586–3616.
  102. Nina, M., Smith, J. & Roux, B. (1993). *Ab initio* quantum-chemical analysis of Schiff-base water interactions in bacteriorhodopsin. *J. Mol. Struct. Theochem*, **105**, 231–245.
  103. Plimpton, S. (1995). Fast parallel algorithms for short-range molecular dynamics. *J. Comput. Phys.* **117**, 1–19.
  104. Woolf, T. B. & Roux, B. (1994). Molecular dynamics simulation of the gramicidin channel in a phospholipid bilayer. *Proc. Natl Acad. Sci. USA*, **91**, 11631–11635.
  105. Woolf, T. B. & Roux, B. (1996). Structure, energetics and dynamics of lipid-protein interactions: a molecular dynamics study of the gramicidin a channel in a DMPC bilayer. *Proteins: Struct. Funct. Genet.* **24**, 92–114.
  106. Woolf, T. B. (1997). Molecular dynamics of individual  $\alpha$ -helices of bacteriorhodopsin in dimyristoyl phosphatidylcholine. I. structure and dynamics. *Biophys. J.* **73**, 2376–2392.
  107. White, S. & Wimley, W. (1999). Membrane protein folding and stability: physical principles. *Annu. Rev. Biophys. Biom. Struct.* **28**, 319–365.
  108. Nagle, J. F. & Tristram-Nagle, S. (2000). Structure of lipid bilayers. *Biochim. Biophys. Acta*, **1469**, 159–195.
  109. Ovchinnikov, Y., Abdulaev, N. & Bogachuk, A. (1988). 2 Adjacent cysteine residues in the C-terminal cytoplasmic fragment of bovine rhodopsin are palmitoylated. *FEBS Letters*, **230**, 1–5.
  110. Brightwell, R., Fisk, L., Greenberg, D., Hudson, T., Levenhagen, M., Maccabe, A. & Riesen, R. (2000). Massively parallel computing using commodity components. *Parallel Comput.* **26**, 243–266.

Edited by G. von Heijne

(Received 24 February 2003; received in revised form 19 August 2003; accepted 20 August 2003)